Reduced basis approximation and error bounds for potential flows in parametrized geometries

Gianluigi Rozza *

Massachusetts Institute of Technology, Department of Mechanical Engineering, Room 3-264, 77 Massachusetts Avenue, Cambridge MA, 02142-4307, USA.

Abstract. In this paper we consider (hierarchical, Lagrange) reduced basis approximation and *a posteriori* error estimation for potential flows in affinely parametrized geometries. We review the essential ingredients: i) a Galerkin projection onto a low-dimensional space associated with a smooth "parametric manifold" in order to get a dimension reduction; ii) an efficient and effective greedy sampling method for identification of optimal and numerically stable approximations to have a rapid convergence; iii) an *a posteriori* error estimation procedure: rigorous and sharp bounds for the linear-functional outputs of interest and over the potential solution or related quantities of interest like velocity and/or pressure; iv) an Offline-Online computational decomposition strategies to achieve a minimum *marginal computational cost* for high performance in the real-time and many-query (e.g., design and optimization) contexts. We present three illustrative results for inviscid potential flows in parametrized geometries representing a Venturi channel, a circular bend and an added mass problem.

AMS subject classifications: 65Y20, 76B99, 35Q35, 65N15

Key words: Reduced basis approximation, error bounds, potential flows, Galerkin method, a posteriori error estimation, parametrized geometries.

1 Introduction and motivation

A great number of engineering problems require the solution of partial differential equations (PDEs) for many different configurations of the system. Even the computational costs for the solution of relatively simple parametrized problems may be very high and may remain unaffordable - although the computational power has increased considerably in the past few years. This makes necessary to develop techniques which are able to reduce the complexity of the system without a loss of information or accuracy of the results. The reduced basis method is a promising approach to fill this gap as it allows not only a *rapid* and *efficient*, but also a *reliable* solution of partial differential equations.

*Corresponding author. *Email address:* rozza@mit.edu (G. Rozza).
Currently at Ecole Polytechnique Fédérale de Lausanne, Chair of Modelling and Scientific Computing, Station 8-MA, CH 1015, Lausanne, Switzerland

1.1 The Input-Output Relation

In many applications, the main goal is not only the solution of the PDEs for the *field variables*, but the evaluation of *input-output relationships*. Here, the *output* is expressed as a functional of the field variables and can be for example an average quantity in the domain, an added mass or even a pointwise velocity and/or pressure. The *input-parameter* vector identifies a particular configuration of the system. Usually, this includes geometric variations, but also physical properties as well as boundary/initial conditions and sources. The *field variable* (as solution of the PDEs) connects the input parameters and the outputs of interest.

1.2 The Many-Query and Real-Time Contexts

The reduced basis method allows us to reduce the *online* computational time (both of the field solution and of the outputs of interest) notably. This advantage is gained by additional *offline* effort. Therefore, the methodology presented in this work is suited particularly for problems arising in the *real-time context* or in the *many-query context*. For both these problem classes, the online performance is extremely important while increased offline effort is less critical and both are very challenging to the conventional solution methods. The real-time context arises e.g. for control engineering and in parameter estimation problems in a wide range of applications. Examples for the many-query context are the multi-model/multi-scale simulation or design optimization. Here the online performance is critical because the solution of a huge number of problems - up to the tens of thousands input-output relations - is necessary, making the additional offline effort affordable.
It is important to note that the reduced basis (RB) method can not replace "classical" numerical techniques such as the finite element (FE) method. This is due to two reasons. First, the application of the RB method to problems which require the solution only for one or a few configurations would be inefficient. The reduced online complexity would not balance the offline effort needed for the application of the RB method compared to the FE method (or other solution methods). In addition, the RB method is not an independent method, since it has to be built upon another method for the solution of the particular problem. In fact, the RB method tries to approximate the solution of the system that would be obtained by applying the given underlying solution method to the problem, and not the exact solution. In this work, we will consider a finite element discretization as underlying solution method but also other methods (e.g. finite volume or spectral methods) would be possible. See for example [11,19], applying RB method upon finite volume and spectral methods, respectively.

1.3 Reduced basis background

A brief introduction to the RB background and the most recent developments of the reduced basis method shall be given here. For a more detailed presentation see [49].

The reduced basis method for single parameter problems was first introduced in the late 1970s by Almroth, Stern and Brogan in the domain of nonlinear structural analysis [1]. The method has been developed further by Noor in the following years [27–34] and extended to multiparameter problems. A first *a priori* error analysis for single parameter problems has been carried out by Fink and Rheinboldt [8, 9]. Further work focused on *a priori* error analysis and on different approximation spaces has been done by Porsching [39]. In the 1990s, this topic has been investigated again by Rheinbolt [45] and by Barrett and Reddien [4]. At that time the RB method has been applied to different classes of problems: viscous fluid flow and Navier Stokes equations [38], fluid control problems [14–17], ordinary differential equations [40] and differential algebraic equations [18]. These early methods were typically rather local and low-dimensional in parameter. In [3], Balmes first applied RB methods to general multi-parameter problems. Only recently, the need for reliable *a posteriori* error estimators has led to a number of works on this topic [20–22, 41, 46, 52, 54]. Much effort is devoted to effective sampling strategies for global approximation spaces also for higher dimensional parameter domains [6,26,47]. In the past few years, this methodology has been applied to a wide range of problems including elliptic as well as parabolic and simple hyperbolic problems. Problems came from the field of elasticity, quantum mechanics/chemistry, acoustics, fracture problems, homogenization, Boltzmann models, environmental engineering and inverse problems (for actual works on these topics refer to [2]). Other applications are in fluid flows (e.g. [48, 50, 53]) and in optimization and optimal control (e.g. [10, 35, 42, 48]). Two recent publications give a very comprehensive summary of the methodology developed so far for coercive elliptic PDEs with affine parameter dependence [37, 49].

1.4 Reduced basis method for potential flows

In this paper we will introduce the theory of the reduced basis (RB) method for potential flows in parametrized domains with special error bounds on velocity and pressure. After a short summary of the historical background and recent developments related with the RB method, we will review in Sections 2–3 the relevant steps for the generation of the rapidly convergent global RB approximation spaces and the approximation of the solution for parametrized coercive elliptic PDEs with affine parameter dependence, which enables an efficient offline-online decomposition. *A posteriori* error estimators and lower bounds for the coercivity constant will play an important role in this process (Sect. 4–5). Finally, the geometric parametrizations used in this work (Sect. 6–8) and their application in the RB context will be presented by three potential flow examples (Sect. 10–12).

2 Problem Definition

In this section, we will review the abstract formulation for coercive elliptic PDEs with affine parameter dependence. The methodology of the RB method for potential flows described further in this work will apply to this wide class of problems.

2.1 Exact statement

We consider a suitably regular (smooth) domain $\Omega \subset \mathbb{R}^2$ with Lipschitz-continuous boundary $\partial\Omega$. X^e is an associated (infinite dimensional) Hilbert space satisfying $(H_0^1(\Omega))^\nu \subset X^e \subset (H^1(\Omega))^\nu$, where ν is the dimension of the problem (scalar if $\nu = 1$, vectorial if $\nu > 1$). Here, $H^1(\Omega) = \{v \in L^2(\Omega) | \nabla v \in (L^2(\Omega))^d\}$, $H_0^1(\Omega) = \{v \in H^1(\Omega) | v|_{\partial\Omega} = 0\}$, and $L^2(\Omega) = \{v$ measurable $| \int_\Omega v^2$ finite$\}$. The inner product and norm associated with X^e are given by $(\cdot,\cdot)_{X^e}$ and $\|\cdot\|_{X^e} = (\cdot,\cdot)_{X^e}^{1/2}$, respectively. Additionally, we define an input parameter domain $\mathcal{D} \subset \mathbb{R}^P$. The superscript ^{e} refers to "exact", where the "exact" problem is: for any given parameter $\boldsymbol{\mu} \in \mathcal{D} \subset \mathbb{R}^P$, evaluate the scalar output of interest

$$s^e(\boldsymbol{\mu}) = l(u^e(\boldsymbol{\mu})),$$

where the field variable $u^e(\boldsymbol{\mu}) \in X^e$ satisfies

$$a(u^e(\boldsymbol{\mu}), v; \boldsymbol{\mu}) = f(v), \qquad \forall v \in X^e. \tag{2.1}$$

We assume that the form $a(\cdot,\cdot;\boldsymbol{\mu}) : X^e \times X^e \to \mathbb{R}$ is bilinear, coercive and continuous, and $l(\cdot) : X^e \to \mathbb{R}$ is a bounded linear functional. If $l = f$, we say that our problem is "compliant".

2.2 "Truth" Finite Element approximation

We proceed now to the finite element approximation of (2.1) (see e.g. [7, 43]). We replace X^e with $X^{N_t} \subset X^e$ which is a sequence of (conforming) "truth" finite element approximation spaces of finite but large dimension N_t. The "truth" finite element approximation is: for any given parameter $\boldsymbol{\mu} \in \mathcal{D} \subset \mathbb{R}^P$, evaluate

$$s^{N_t}(\boldsymbol{\mu}) = l(u^{N_t}(\boldsymbol{\mu})),$$

where $u^{N_t}(\boldsymbol{\mu})$ satisfies

$$a(u^{N_t}(\boldsymbol{\mu}), v; \boldsymbol{\mu}) = f(v), \qquad \forall v \in X^{N_t}. \tag{2.2}$$

Our "truth" FE approximation $u^{N_t}(\boldsymbol{\mu}) \in X^{N_t}$ to $u^e(\boldsymbol{\mu})$ is thus defined as the Galerkin projection of $u^e(\boldsymbol{\mu})$ onto X^{N_t}. The finite element discretization shall be assumed to be sufficiently rich such that $u^{N_t}(\boldsymbol{\mu})$ and $s^{N_t}(\boldsymbol{\mu})$ are sufficiently close to $u^e(\boldsymbol{\mu})$ resp. $s^e(\boldsymbol{\mu})$ - this is the reason why we call it "truth" approximation. The RB field solution and RB output shall approximate this "truth" finite element field solution $u^{N_t}(\boldsymbol{\mu})$ and output $s^{N_t}(\boldsymbol{\mu})$ and not the "exact" solutions $u^e(\boldsymbol{\mu})$ and $s^e(\boldsymbol{\mu})$. The reduced basis error will thus be evaluated with respect to the "truth" finite element solutions. Our method remains computationally stable and efficient as $N_t \to \infty$. We will define two different inner products and norms for members of X^{N_t}, inherited from X^e. First, an energy inner product and energy norm defined respectively as $(w,v)_{\boldsymbol{\mu}} \equiv a(w,v;\boldsymbol{\mu})$, $\forall w,v \in X^e$ and $\|w\|_{\boldsymbol{\mu}} \equiv (w,w)_{\boldsymbol{\mu}}^{1/2}$, $\forall w \in X^e$.
Second, the X^{N_t} (resp. X^e) inner product and norm, are defined as follows: for given $\overline{\boldsymbol{\mu}} \in \mathcal{D}$ and (non-negative) real τ, $(w,v)_X \equiv (w,v)_{\overline{\boldsymbol{\mu}}} + \tau(w,v)_{L^2(\Omega)}$, $\forall w,v \in X^e$ and $\|w\|_X \equiv (w,w)_X^{1/2}$, $\forall w \in X^e$. The L^2-norm is defined as $(w,v)_{L^2(\Omega)} \equiv \int_\Omega wv$.

2.3 Well Posedness

We define our exact and FE coercivity constants as

$$\alpha^e(\boldsymbol{\mu}) = \inf_{w \in X^e} \frac{a(w,w;\boldsymbol{\mu})}{\|w\|_X^2}, \quad \alpha^{N_t}(\boldsymbol{\mu}) = \inf_{w \in X^{N_t}} \frac{a(w,w;\boldsymbol{\mu})}{\|w\|_X^2}. \tag{2.3}$$

As we assumed that our bilinear form is coercive and our FE approximation spaces are conforming, it follows that $\alpha^{N_t}(\boldsymbol{\mu}) \geq \alpha^e(\boldsymbol{\mu}) \geq \alpha_0 > 0, \forall \boldsymbol{\mu} \in \mathcal{D}$. The continuity constants are defined similarly as

$$\gamma^e(\boldsymbol{\mu}) = \sup_{w \in X^e} \sup_{v \in X^e} \frac{a(w,v;\boldsymbol{\mu})}{\|w\|_X \|v\|_X}, \quad \gamma^{N_t}(\boldsymbol{\mu}) = \sup_{w \in X^{N_t}} \sup_{v \in X^{N_t}} \frac{a(w,v;\boldsymbol{\mu})}{\|w\|_X \|v\|_X}. \tag{2.4}$$

It is clear from our continuity and conforming hypotheses that $\gamma^{N_t}(\boldsymbol{\mu}) \leq \gamma^e(\boldsymbol{\mu}) \leq \gamma_0 < \infty$, $\forall \boldsymbol{\mu} \in \mathcal{D}$. If the bilinear form a fulfills these requirements of coercivity and continuity and if the linear form f is bounded, the system (2.1) has a unique solution.

2.4 Affine Parameter Dependence

We also make an important assumption on the nature of the parametric depedence of the problem. In particular, we suppose that the parametric bilinear form a is "affine" in the parameter $\boldsymbol{\mu}$; this means that it can be expressed as

$$a(w,v;\boldsymbol{\mu}) = \sum_{q=1}^{Q_a} \Theta_a^q(\boldsymbol{\mu}) a^q(w,v), \quad \forall w,v \in X^{N_t}, \forall \boldsymbol{\mu} \in \mathcal{D}, \tag{2.5}$$

where Q_a should be a finite and preferably small integer. The functions $\Theta_a^q(\boldsymbol{\mu}) : \mathcal{D} \to \mathbb{R}$ depend on $\boldsymbol{\mu}$ and are typically very smooth, while the bilinear forms $a^q(\cdot,\cdot) : X^e \times X^e \to \mathbb{R}$ are $\boldsymbol{\mu}$-independent X^e-continuous bilinear forms. The linear form f may also depend affinely on the parameter and can in this case be expressed as a sum of Q^f producs of parameter-dependent functions and parameter-independent X^e-bounded linear forms.

The assumption of affine parameter dependence is crucial for the computational performance of our method as it allows an efficient offline-online decomposition of the relevant computational procedures. In fact, this assumption is not too restrictive as there exist many applications with both geometric and property variations which exhibit an affine dependence on the parameter. Some examples are shown with numerical results.

3 Reduced Basis Approximation

Sections 3–5 contain a review on RB methodology recalling the main features at the state of the art (a priori convergence, a posteriori error bounds and adaptive procedures for basis assembling). The expert reader may go directly to Section 6 for more details on geometrical parametrizations or to Sections 7–8 for original elements dealing with potential flows and their applications.

The parametric real-time and many-query settings introduced before represent two different computational opportunities. The first opportunity is the fact that in the parametric setting our attention can be restricted to a typically smooth and rather low-dimensional parametrically induced manifold, which is much smaller than the unnecessarily rich generic approximation spaces of e.g. the FE method. The second opportunity is - as mentioned before - that an increased offline time can be accepted in these contexts if the online evaluation time of the input-output relation is reduced considerably in exchange. In the following, we will describe the main steps of the reduced basis method with a special attention to these two opportunities.

3.1 Manifold of Solutions

As noted above, the field variable $u^e(\boldsymbol{\mu})$ is not an arbitrary member of the infinite–dimensional solution space X^e associated with the underlying partial differential equation. In fact, it resides on a much lower-dimensional and typically smooth manifold $M \equiv \{u^e(\boldsymbol{\mu})|\boldsymbol{\mu}\in\mathcal{D}\}$ induced by the parametric dependence. For example, in the case of a single parameter $\boldsymbol{\mu}\in\mathcal{D}\subset\mathbb{R}^{P=1}$, $u^e(\boldsymbol{\mu})$ describes a one-dimensional filament that winds through X^e. This situation is depicted in Figure 1. Thus, the possible solutions $u^e(\boldsymbol{\mu})$ do not cover the entire space X^e, which means that this space is too general as it can represent a much wider range of functions.

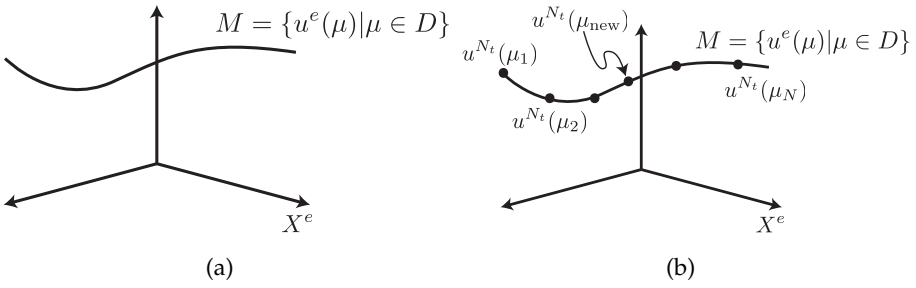

Figure 1: (a) Low-dimensional manifold on which the field variable resides and (b) approximation of a new solution at $\boldsymbol{\mu}_{\text{new}}$ with the "snapshots" $u^{N_t}(\boldsymbol{\mu}_n), 1\leq n\leq N$.

The "truth" finite element approximation space X^{N_t} is constructed to approximate all members of X^e. It is therefore still much too general as it includes many functions which do not reside on the manifold of interest M. To approximate $u^{N_t}(\boldsymbol{\mu})$ by an adjusted method, it is sufficient to be able to approximate all functions which lie on M while it is not necessary to represent every single function in X^{N_t}. If we exploit this observation and restrict our attention and adjusted approximation space to the parameter-induced low-dimensional solution manifold, we can effect substantial dimension reduction and considerable computational economies.

The basic idea is to construct a special approximation space for the manifold M by using the pre-computed solutions $u^{N_t}(\boldsymbol{\mu_n})$ at $N\ll N_t$ selected points $\boldsymbol{\mu_n}$ along M, as shown in

Figure 1. The solution $u^N(\boldsymbol{\mu}_{new})$ at a newly chosen point $\boldsymbol{\mu}_{new}$ can then be approximated by taking an appropriate linear combination of the sample points $u^{N_t}(\boldsymbol{\mu}_n), 1 \leq n \leq N$, which means by a projection onto the adjusted approximation space.

3.2 RB Spaces

The starting point is the FE approximation space of dimension N_t, X^{N_t}. We then want to construct an associated sequence of hierarchical approximation spaces with maximum dimension $N_{\max}$, $X_N^{N_t}, N = 1,..,N_{\max}$. Each of these spaces is an N-dimensional subspace of X^{N_t}. Hierarchical means that the spaces are such that $X_1^{N_t} \subset X_2^{N_t} \subset \ldots \subset X_{N_{\max}}^{N_t} \subset X^{N_t}$; this quality will play an important role for computational and memory efficiency.

In this work, we will only use Lagrange reduced basis spaces [39]. It is possible to work with Taylor [31,39] and Hermite [15] spaces as well and much of the methodology does not change for these spaces. We first introduce - for given $N \in \{1,\ldots,N_{\max}\}$ - a set of nested samples in parameter space,

$$S_N = \{\boldsymbol{\mu}_1 \in \mathcal{D}, \ldots, \boldsymbol{\mu}_N \in \mathcal{D}\}, \quad 1 \leq N \leq N_{\max}, \tag{3.1}$$

such that $S_1 \subset \cdots \subset S_N \subset S_{N_{\max}}$ (the parameter samples are nested). The associated Lagrange RB approximation spaces are then given as

$$W_N^{N_t} = \text{span}\{u^{N_t}(\boldsymbol{\mu}_n), \quad 1 \leq n \leq N\}, \quad 1 \leq N \leq N_{\max}, \tag{3.2}$$

where $u^{N_t}(\boldsymbol{\mu}_n) \in X^{N_t}$ is the solution to (2.2) for $\boldsymbol{\mu} = \boldsymbol{\mu}_n$. By construction, the Langrange RB spaces are hierarchical: $W_1^{N_t} \subset W_2^{N_t} \subset \cdots \subset W_{N_{\max}}^{N_t} \subset X^{N_t}$. The $u_n^{N_t} = u^{N_t}(\boldsymbol{\mu}_n), 1 \leq n \leq N_{\max}$ are often called "snapshots" or, more precisely, "retained snapshots" of the parametric manifold M. The next question we have to address is how we can choose a good combination of the retained snapshots to approximate the solution for a new parameter value and how we can build a stable RB basis out of the retained snapshots.

3.3 Galerkin Projection

Given our hypotheses on a and f, a Galerkin projection gives the reduced basis approximation $u_N^{N_t}(\boldsymbol{\mu})$: for any $\boldsymbol{\mu} \in \mathcal{D}$, $u_N^{N_t}(\boldsymbol{\mu}) \in W_N^{N_t}$ satisfies

$$a(u_N^{N_t}(\boldsymbol{\mu}), v; \boldsymbol{\mu}) = f(v), \qquad \forall v \in X_N^{N_t}. \tag{3.3}$$

We then evaluate

$$s_N^{N_t}(\boldsymbol{\mu}) = l(u_N^{N_t}(\boldsymbol{\mu})). \tag{3.4}$$

In theory, we can choose as Lagrange sample points (3.1) any set of parameter values that induce a linearly independent set of retained snapshots (3.2). However, the snapshots will become more and more colinear as N increases because of the rapid convergence of the Lagrange space: if $W_N^{N_t}$ is already able to approximate well any member of M, then the next snapshot $u_{N+1}^{N_t}(\boldsymbol{\mu})$ will be "almost" linearly dependent of the members of the "old"

space $W_N^{N_t}$. The direct choice of the retained snapshots as basis functions would therefore lead to a very poorly conditioned equation system for the solution of (3.3). To create a well-conditioned set of basis functions, we will therefore apply the Gram-Schmidt process in the $(\cdot,\cdot)_X$ inner product to our set of snapshots $u_N^{N_t}(\boldsymbol{\mu}_n), 1 \le n \le N_{\max}$. This process will return a mutually orthogonal set of basis functions $\zeta_n^{N_t}, 1 \le n \le N_{\max}$ which we can choose as our bases for $W_N^{N_t}$ (resp. $X_N^{N_t}$). These basis functions will fulfilll the orthonormality condition

$$(\zeta_n^{N_t}, \zeta_m^{N_t})_X = \delta_{n,m}, \qquad 1 \le n,m \le N_{\max}, \tag{3.5}$$

where $\delta_{n,m}$ is the Kronecker-delta symbol. This orthogonality condition is necessary to ensure a well-conditioned reduced basis algebraic system. The orthonormalization process is given as follows [37]:

$$\begin{aligned}
&\zeta_1^{N_t} = u_1^{N_t} / \|u_1^{N_t}\|_X; \\
&\texttt{for } n = 2 : N_{\max} \\
&\quad z_n^{N_t} = u_n^{N_t} - \sum_{m=1}^{n-1} (u_n^{N_t}, \zeta_m^{N_t})_X \zeta_m^{N_t}; \\
&\quad \zeta_n^{N_t} = z_n^{N_t} / \|z_n^{N_t}\|_X; \\
&\texttt{end.}
\end{aligned} \tag{3.6}$$

The discrete equations associated to the Galerkin system (3.3) are then constructed by inserting the expansion of $u_N^{N_t}(\boldsymbol{\mu})$ in the basis functions

$$u_N^{N_t}(\boldsymbol{\mu}) = \sum_{m=1}^{N} u_{Nm}^{N_t}(\boldsymbol{\mu}) \zeta_m^{N_t} \tag{3.7}$$

and $v = \zeta_n^{N_t}, 1 \le n \le N$ into (3.3). The equation obtained is the reduced basis stiffness equation for the reduced basis coefficients $u_{Nm}^{N_t}(\boldsymbol{\mu}), 1 \le m \le N$:

$$\sum_{m=1}^{N} a(\zeta_m^{N_t}, \zeta_n^{N_t}; \boldsymbol{\mu}) u_{Nm}^{N_t}(\boldsymbol{\mu}) = f(\zeta_n^{N_t}), \quad 1 \le n \le N. \tag{3.8}$$

The reduced basis output prediction can then be evaluated as

$$s_N^{N_t}(\boldsymbol{\mu}) = \sum_{m=1}^{N} u_{Nm}^{N_t}(\boldsymbol{\mu}) l(\zeta_m^{N_t}). \tag{3.9}$$

As shown in [37], the condition number of the matrix $a(\zeta_m^{N_t}, \zeta_n^{N_t}; \boldsymbol{\mu}), 1 \le n,m \le N$, is independent of N and N_t and bounded by $\gamma^e(\boldsymbol{\mu}) / \alpha^e(\boldsymbol{\mu})$.

3.4 Offline-Online Procedure

System (3.8) has normally a very small size (and a full structure) compared to the system that arises from standard FE discretization of (2.2), since it consists of a set of N linear algebraic equations in N unknowns, while the FE discretization would lead to a set of $N_t \gg N$ equations in $N_t \gg N$ unkowns. Nevertheless, the elements of $W_N^{N_t}$, the basis functions $\zeta_n^{N_t}, 1 \le n \le N$, are associated with the underlying FE space and thus N_t-dependent.

This makes the formation of the stiffness matrix and the load vector for our RB system (3.8), for every new value of $\boldsymbol{\mu}$ N_t-dependent, even though the solution of this system is not. To eliminate this N_t-dependency, which would lead to a very poor online performance, we construct a very efficient offline-online procedure. This procedure is based on the affine parameter dependence, as we now discuss. Equation (2.5) allows us to express our system (3.8) as

$$\sum_{m=1}^{N}\left(\sum_{q=1}^{Q_a}\Theta^q(\boldsymbol{\mu})a^q(\zeta_m^{N_t},\zeta_n^{N_t})\right)u_{Nm}^{N_t}(\boldsymbol{\mu})=f(\zeta_n^{N_t}),\quad 1\le n\le N. \tag{3.10}$$

If f is also affinely dependent on the parameter $\boldsymbol{\mu}$, the right hand side of this equation can be expanded in a similar sum of Q_f affine terms, but in the following discussion we will assume that f does not depend on $\boldsymbol{\mu}$. We see that the terms dependent on the $\zeta_n^{N_t}$ are now separated of those dependent on the parameter. Therefore we can precompute all terms independent of the parameter in the offline stage and thus the operation count for the online computations is independent of N_t.

In the *offline stage* - performed only once - we first compute the $u^{N_t}(\boldsymbol{\mu}_n), 1\le n\le N_{\max}$ and form the $\zeta_n^{N_t}, 1\le n\le N_{\max}$. After that,

$$f(\zeta_n^{N_t}),\quad 1\le n\le N_{\max} \tag{3.11}$$

and

$$a^q(\zeta_m^{N_t},\zeta_n^{N_t}),\quad 1\le n,m\le N_{\max},\quad 1\le q\le Q_a \tag{3.12}$$

can be computed and stored. This requires $\mathcal{O}(Q_a N_{\max}^2 N_t)$ operations and $\mathcal{O}(Q_a N_{\max}^2)$ storage. In the *online stage* - performed many times, for each new value of $\boldsymbol{\mu}$ - we use the precomputed matrices (3.12) to assemble the (full) $N\times N$ stiffness matrix

$$\sum_{q=1}^{Q_a}\Theta^q(\boldsymbol{\mu})a^q(\zeta_m^{N_t},\zeta_n^{N_t}),\quad 1\le n,m\le N. \tag{3.13}$$

We then solve the resulting system (3.10) to obtain the $u_{Nm}^{N_t}(\boldsymbol{\mu}), 1\le m\le N$ and evaluate the output approximation (3.9). The operation count for the online stage is then $\mathcal{O}(Q_a N^2)$ to assemble (3.12), $\mathcal{O}(N^3)$ to invert the full stiffness matrix and $\mathcal{O}(N)$ to evaluate the inner product for the output computation. Thanks to the hierarchical condition, the online storage is only $\mathcal{O}(Q_a N_{\max}^2)+\mathcal{O}(N_{\max})$, as for any given N the necessary RB $N\times N$ matrices may be extracted of the corresponding "maximum" $N_{\max}\times N_{\max}$ system. The crucial point is that our online computational costs are dependent on Q_a and N, but independent of N_t. Since $N\ll N_t$, we can expect significant (orders of magnitude) speedup in the online stage compared to the pure FE approach. This implies also that we may choose N_t very large in order to eliminate the error between the exact solution and the FE predictions without affecting the reduced basis online efficiency. In fact, the bigger the underlying FE system and thus N_t is chosen, the bigger the speedup by the use of the RB method in the online stage will be. However, we should keep in mind that the offline phase is still N_t-dependent.

3.5 Sampling Strategy: a "Greedy" Algorithm

The question we deal with in this section is how to choose the sample points $\boldsymbol{\mu}_n, 1 \le n \le N$ for a given N in an optimal way, such that the accuracy of the resulting RB approximation is maximized. The key ingredient is a rigourous, sharp and inexpensive a posteriori error bound $\Delta_N^{N_t}(\boldsymbol{\mu})$ (defined later in (4.8)–(4.9)) such that

$$\|u^{N_t}(\boldsymbol{\mu}) - u_N^{N_t}(\boldsymbol{\mu})\|_X \le \Delta_N^{N_t}(\boldsymbol{\mu}) \tag{3.14}$$

for all $\boldsymbol{\mu} \in D$ and for all N. The properties of sharpness and rigor can be quantified by introducing the effectivity

$$\eta_N^{N_t}(\boldsymbol{\mu}) \equiv \frac{\Delta_N^{N_t}(\boldsymbol{\mu})}{\|u^{N_t}(\boldsymbol{\mu}) - u_N^{N_t}(\boldsymbol{\mu})\|_X}. \tag{3.15}$$

Rigor means that we require that $\Delta_N^{N_t}(\boldsymbol{\mu})$ is never less than the true error. Sharpness means that we require that $\Delta_N^{N_t}(\boldsymbol{\mu})$ is not too much larger than the true error. To put this into one equation, $\Delta_N^{N_t}(\boldsymbol{\mu})$ must fulfilll $1 \le \eta_N^{N_t}(\boldsymbol{\mu}) \le \eta_{\text{max, UB}}, \forall \boldsymbol{\mu} \in \mathcal{D}, 1 \le N \le N_{\max}$, where $\eta_{\text{max, UB}}$ is finite (preferably close to 1) and independent of N. The computation of the error bound is "inexpensive" if we can compute $\boldsymbol{\mu} \to \Delta_N^{N_t}(\boldsymbol{\mu})$ extremely fast, which implies that in the limit of many evaluations the marginal cost is independent of N_t. We discuss the construction and properties of such an error estimate in detail in section 4. We will now proceed to the "greedy" procedure which makes use of this a posteriori error estimate to construct hierarchical Lagrange RB approximation spaces.

We are given $N_{\max}$, which can be set either directly or through a prescribed error tolerance ϵ_{tol}, and a training sample $\Xi_{\text{train}} \subset \mathcal{D}$ (a discrete set representing a very fine sample of $n_{\text{train}} = |\Xi_{\text{train}}|$ points in the parameter domain). This "training" sample shall serve as surrogate for $\mathcal{D}$ in the subsequent generation of the reduced basis space and the choice of n_{train} and Ξ_{train} has therefore important offline and online computational implications. We then choose at random $\boldsymbol{\mu}_1 \in \Xi_{\text{train}}$, the first sample point to be added to the Lagrange parameter samples $S_1 = \{\boldsymbol{\mu}_1\}$, and set $W_1^{N_t\text{Greedy}} = \text{span}\{u^{N_t}(\boldsymbol{\mu}_1)\}$. The algorithm proceeds as follows:

$$\begin{aligned}
&\texttt{for } N = 2 : N_{\max} \\
&\quad \boldsymbol{\mu}_N = \arg\max_{\boldsymbol{\mu} \in \Xi_{\text{train}}} \Delta_{N-1}^{N_t}(\boldsymbol{\mu}); \\
&\quad \epsilon_{N-1} = \Delta_{N-1}^{N_t}(\boldsymbol{\mu}_N); \\
&\quad \texttt{if } \epsilon_{N-1} \le \epsilon_{\text{tol}} \\
&\qquad N_{\max} = N - 1; \\
&\quad \texttt{end;} \\
&\quad S_N^{N_t} = S_{N-1} \cup \boldsymbol{\mu}_N, \\
&\quad W_N^{N_t\text{Greedy}} = W_{N-1}^{N_t\text{Greedy}} + \text{span}\{u^{N_t}(\boldsymbol{\mu}_N)\} \\
&\texttt{end.}
\end{aligned} \tag{3.16}$$

Hence, the greedy algorithm chooses in each iteration N that particular candidate snapshot (over all candidate snapshots $u^{N_t}(\boldsymbol{\mu}), \boldsymbol{\mu} \in \Xi_{\text{train}}$) which is worst well approximated by the projection on the "old" RB space $W_{N-1}^{N_t \text{greedy}}$ and appends it to the retained snapshots. The most crucial point of this strategy is that the error is not measured by the (very expensive) "true" error $\|u^{N_t}(\boldsymbol{\mu}) - u_N^{N_t}(\boldsymbol{\mu})\|_X$ but by the inexpensive a posteriori error bound $\Delta_N^{N_t}(\boldsymbol{\mu})$. In doing so we need to compute only the $N_{\max}$ (typically very few) FE retained snapshots[†]. This permits us to perform offline a very exhaustive search for the best sample with n_{train} very large and thus get most rapidly uniformly convergent spaces $W_N^{N_t \text{Greedy}}$. Online, we can exploit the low marginal cost of the error estimate and the hierarchical condition of the $W_N^{N_t \text{Greedy}}, 1 \le N \le N_{\max}$ to determine the smallest N (the most efficient approximation) for which we rigorously achieve the desired accuracy.

3.6 Convergence Analysis

We will now re-state some theoretical evidence that the reduced basis approximation indeed converges to the FE approximation, if a good low-dimensional approximation space exists and consequently a good Lagrange RB approximation space can be constructed by the greedy algorithm. In addition, results shall be presented that confirm the existence of suited RB approximation spaces and provide upper bounds for convergence rates in terms of the given data for the problem.

3.6.1 Optimality

First, the classical Galerkin optimality result for the projection in the RB approximation space shall demonstrated:

$$\|u^{N_t}(\boldsymbol{\mu}) - u_N^{N_t}(\boldsymbol{\mu})\|_{\boldsymbol{\mu}} = \inf_{w_N \in X_N^{N_t}} \|u^{N_t}(\boldsymbol{\mu}) - w_N(\boldsymbol{\mu})\|_{\boldsymbol{\mu}}, \tag{3.17}$$

$$\|u^{N_t}(\boldsymbol{\mu}) - u_N^{N_t}(\boldsymbol{\mu})\|_X = \sqrt{\frac{\gamma^e(\boldsymbol{\mu})}{\alpha^e(\boldsymbol{\mu})}} \inf_{w_N \in X_N^{N_t}} \|u^{N_t}(\boldsymbol{\mu}) - w_N(\boldsymbol{\mu})\|_X, \tag{3.18}$$

and for the compliant case also

$$s^{N_t}(\boldsymbol{\mu}) - s_N^{N_t}(\boldsymbol{\mu}) = \|u^{N_t}(\boldsymbol{\mu}) - u_N^{N_t}(\boldsymbol{\mu})\|_{\boldsymbol{\mu}}^2 = \inf_{w_N \in X_N^{N_t}} \|u^{N_t}(\boldsymbol{\mu}) - w_N(\boldsymbol{\mu})\|_{\boldsymbol{\mu}}^2, \tag{3.19}$$

as well as

$$0 < s^{N_t}(\boldsymbol{\mu}) - s_N^{N_t}(\boldsymbol{\mu}) \le \gamma^e(\boldsymbol{\mu}) \inf_{w_N \in X_N^{N_t}} \|u^{N_t}(\boldsymbol{\mu}) - w_N(\boldsymbol{\mu})\|_X^2. \tag{3.20}$$

To prove (3.17), we first state, since our reduced basis space is conforming, $X_N^{N_t} \subset X^{N_t}$, the Galerkin orthogonality: indicating as $e(\boldsymbol{\mu}) := u^{N_t}(\boldsymbol{\mu}) - u_N^{N_t}(\boldsymbol{\mu}) \in X^{N_t}$, we have that

$$a(e(\boldsymbol{\mu}), v; \boldsymbol{\mu}) = a(u^{N_t}(\boldsymbol{\mu}) - u_N^{N_t}(\boldsymbol{\mu}), v; \boldsymbol{\mu}) = 0, \quad \forall v \in X_N^{N_t}. \tag{3.21}$$

[†]This is contrary to the proper orthogonal decomposition (POD) approach, where we have to compute the FE solutions for all members of Ξ_{train} as we measure the error by the true error $\|u^{N_t}(\boldsymbol{\mu}) - u_N^{N_t}(\boldsymbol{\mu})\|_X$, see [37, 49].

It then follows that for any $w_N = u_N^{N_t} + v_N \in X_N^{N_t}$ ($v_N \neq 0$),

$$\begin{aligned} a(u^{N_t}(\boldsymbol{\mu}) - w_N, u^{N_t}(\boldsymbol{\mu}) - w_N; \boldsymbol{\mu}) &= a(u^{N_t}(\boldsymbol{\mu}) - u_N^{N_t}(\boldsymbol{\mu}) - v_N, u^{N_t} - u_N^{N_t}(\boldsymbol{\mu}) - v_N; \boldsymbol{\mu}) \\ &= a(u^{N_t}(\boldsymbol{\mu}) - u_N^{N_t}(\boldsymbol{\mu}), u^{N_t}(\boldsymbol{\mu}) - u_N^{N_t}(\boldsymbol{\mu}); \boldsymbol{\mu}) - 2a(u^{N_t}(\boldsymbol{\mu}) - u_N^{N_t}(\boldsymbol{\mu}), v_N; \boldsymbol{\mu}) + a(v_N, v_N; \boldsymbol{\mu}) \\ &\geq a(u^{N_t}(\boldsymbol{\mu}) - u_N^{N_t}(\boldsymbol{\mu}), u^{N_t}(\boldsymbol{\mu}) - u_N^{N_t}(\boldsymbol{\mu}); \boldsymbol{\mu}) \end{aligned} \tag{3.22}$$

from (3.21), symmetry of a and coercivity (2.3). Inequality (3.17) in the energy norm then follows directly. To obtain the result in the X-norm (3.18), we apply the energy-norm bound (3.17) together with coercivity and continuity. The output result (3.19) is found by invoking compliance and Galerkin orthogonality (considering a "compliant" case, $s^{N_t}(\boldsymbol{\mu}) - s_N^{N_t}(\boldsymbol{\mu}) = f(e(\boldsymbol{\mu})) = a(u^{N_t}(\boldsymbol{\mu}), e(\boldsymbol{\mu}); \boldsymbol{\mu}) = a(e(\boldsymbol{\mu}), e(\boldsymbol{\mu}); \boldsymbol{\mu})$) and then using again the energy-norm bound (3.17). The result (3.20) follows from (3.19) and continuity.

The output approximation $s_N^{N_t}(\boldsymbol{\mu})$ thus converges to $s^{N_t}(\boldsymbol{\mu})$ as the square of the error in the field variable $u_N^{N_t}$. We also note that $s_N^{N_t}(\boldsymbol{\mu})$ is a lower bound for $s^{N_t}(\boldsymbol{\mu})$.

3.6.2 A brief comment on a priori convergence theory

We briefly review some results about a priory convergence theory for problems with one parameter ($P = 1$), see for more details and proofs [23,24,37]. First, we define the parameter domain $\mathcal{D} = [\mu_{\min}, \mu_{\max}]$, and $\mu_r = \mu_{max} / \mu_{min}$. We introduce then the non-hierarchical Lagrange equi-ln spaces $W^{N_t ln}, 1 \leq N \leq N_{\max}$, given by $W_N^{N_t ln} = \text{span}\{u^{N_t}(\mu_N^n), 1 \leq n \leq N\}$, for the parameter points given by

$$\mu_N^n = \mu_{\min} \exp\left(\frac{n-1}{N-1} \ln \mu_r\right), \quad 1 \leq n \leq N \leq N_{\max}. \tag{3.23}$$

These spaces contain certain optimality properties as the a priori theory suggests. Denoting by $u_N^{N_t ln}$ the corresponding RB approximations, we obtain the following result: for any $N \geq N_{\text{crit}}$ and $\forall \mu \in \mathcal{D}$,

$$\frac{\|u^{N_t}(\mu) - u_N^{N_t ln}(\mu)\|_{\boldsymbol{\mu}}}{\|u^{N_t}(\mu)\|_{\boldsymbol{\mu}}} \leq \exp\left(-\frac{N-1}{N_{\text{crit}}-1}\right), \tag{3.24}$$

where $N_{\text{crit}} = 1 + [2e \ln \mu_r]_+$. Here, $[\cdot]_+$ returns the smallest integer greater than or equal to its real argument. This result leads to several important conclusions [37,49].

First, the interpretation of RB approximation in a "parameter domain" analogue to FE approximation in the "physical domain" has also a quantitative relevance. Second, while FE convergence relies on spatial regularity, RB convergence is based on smoothness in parameter and discontinuities in space may be allowed. Third, the RB convergence rate upper bound (3.24) does not depend on N_t. The actual convergence rate however does depend on the underlyding FE approximation space, but this dependence vanishes as N_t increases for any fixed N. The next conclusion is that the RB convergence rate depends only relatively weakly on the extent of the parameter domain as the exponent in the convergence rate decreases only logarithmically with μ_r. Last, we can confirm that the RB approximation can converge very quickly (exponentially).

For higher parameter dimensions $P > 1$, there is unfortunately no any closed a priori convergence theory. Numerical examinations show however that there is a very rapid convergence also in this case (the convergence rate with N appears to depend only weakly on P) and that the RB method can in fact treat problems with "many" parameters.

4 A Posteriori Error Estimation

In this section we deal with a posteriori error estimation in the reduced basis context for affinely parametrized elliptic coercive PDEs by an offline-online procedure decomposition to guarantee an efficient and reliable computation. Concerning efficiency both the offline and online computational procedure benefit from the application of error bounds. As already mentioned before, the greedy algorithm can use a significantly larger training sample with (at the same time) considerably decreased computational costs if a posteriori error estimators are used instead of the real error. This leads to a better accuracy of the reduced basis approximation which can be achieved with a smaller number N of basis functions - this means that we have in turn computational savings in the online stage. Another possiblity to save online computational time is to use the error bounds directly in the online stage to find the smallest RB dimension N that allows us to achieve a certain prescribed accuracy. To sum up, the a posteriori error bounds are an essential tool to control the error and hence to minimize the computational costs.

The second keyword - reliability - has a more direct connection to error bounds. As the offline sampling procedures only work with a finite training set of parameter points, the error for large parts of our parameter domain $\mathcal{D}$ remains uncharacterized. By the help of an efficient a posteriori error bound, we can make up for this error quantification for each new parameter value $\boldsymbol{\mu}$ in the online stage and thus can make sure that constraints are satisfied, feasibility (and safety/failure) conditions are verified and prognoses are valid (in each case not only for the RB approximation but for the "truth" FE solution). That means that we do not loose any confidence in the solution compared to the underlying FE solution while exploiting the rapid predictive power of the RB approximation.

In addition, the pre-asymptotic and essentially ad hoc or empirical nature of reduced basis discretization together with the fact that the RB basis functions can not be directly related to any spatial or temporal scales (which makes physical intuiton of little value), and the special needs of deployed real-time systems virtually demand rigorous a posteriori error bounds.

4.1 Preliminaries

We introduce two basic ingredients of our error bounds: the error residual relationship and coercivity lower bounds. The residual $r(v;\boldsymbol{\mu}) \in (X^{N_t})'$ (the dual space to X^{N_t}) is defined as

$$r(v;\boldsymbol{\mu}) \equiv f(v;\boldsymbol{\mu}) - a(u_N^{N_t}(\boldsymbol{\mu}),v;\boldsymbol{\mu}), \quad \forall v \in X^{N_t}. \tag{4.1}$$

Together with

$$f(v;\boldsymbol{\mu}) = a(u^{N_t},v;\boldsymbol{\mu}), \quad \forall v \in X^{N_t}, \tag{4.2}$$

and the bilinearity of a, we can establish the error residual relationship for the error $e(\boldsymbol{\mu}) = u^{N_t}(\boldsymbol{\mu}) - u_N^{N_t}(\boldsymbol{\mu}) \in X^{N_t}$:

$$a(e(\boldsymbol{\mu}),v;\boldsymbol{\mu}) = r(v;\boldsymbol{\mu}), \quad \forall v \in X^{N_t}. \tag{4.3}$$

We will also introduce the Riesz representation of $r(v;\boldsymbol{\mu})$: $\hat{e}(\boldsymbol{\mu}) \in X^{N_t}$ [37] satisfies

$$(\hat{e}(\boldsymbol{\mu}),v)_X = r(v;\boldsymbol{\mu}), \quad \forall v \in X^{N_t}. \tag{4.4}$$

This allows us to write (4.3) as

$$a(e(\boldsymbol{\mu}),v;\boldsymbol{\mu}) = (\hat{e}(\boldsymbol{\mu}),v)_X, \quad \forall v \in X^{N_t}, \tag{4.5}$$

and it follows that the dual norm of the residual can be evaluated through the Riesz representation:

$$\|r(\cdot,\boldsymbol{\mu})\|_{(X^{N_t})'} \equiv \sup_{v \in X^{N_t}} \frac{r(v;\boldsymbol{\mu})}{\|v\|_X} = \|\hat{e}(\boldsymbol{\mu})\|_X. \tag{4.6}$$

This shall prove to be important for the offline-online decomposition procedures. As a second ingredient, we need a positive lower bound $\alpha_{LB}^{N_t}(\boldsymbol{\mu})$ for $\alpha^{N_t}(\boldsymbol{\mu})$:

$$0 \le \alpha_{LB}^{N_t}(\boldsymbol{\mu}) \le \alpha^{N_t}(\boldsymbol{\mu}) \quad \forall \boldsymbol{\mu} \in \mathcal{D}, \tag{4.7}$$

where the online computational time to evaluate $\boldsymbol{\mu} \to \alpha_{LB}^{N_t}(\boldsymbol{\mu})$ has to be independent of N_t in order to fulfill the efficiency requirements on the error bounds articulated before.

4.2 Error Bounds

We define our error estimator for the energy norm as:

$$\Delta_N^{\text{en}}(\boldsymbol{\mu}) \equiv \frac{\|\hat{e}(\boldsymbol{\mu})\|_X}{\sqrt{\alpha_{LB}^{N_t}(\boldsymbol{\mu})}}. \tag{4.8}$$

An equivalent estimator for the output error is defined as

$$\Delta_N^{s}(\boldsymbol{\mu}) \equiv \frac{\|\hat{e}(\boldsymbol{\mu})\|_X^2}{\alpha_{LB}^{N_t}(\boldsymbol{\mu})}. \tag{4.9}$$

We also introduce the effectivities associated to these error estimators in the energy norm, analogue to (3.15), that help us to quantify *rigor* and *sharpness* and thus the quality of the proposed estimator:

$$\eta_N^{\text{en}}(\boldsymbol{\mu}) \equiv \frac{\Delta_N^{\text{en}}}{\|u^{N_t}(\boldsymbol{\mu}) - u_N^{N_t}(\boldsymbol{\mu})\|_{\boldsymbol{\mu}}}, \tag{4.10}$$

and

$$\eta_N^{s}(\boldsymbol{\mu}) \equiv \frac{\Delta_N^{s}(\boldsymbol{\mu})}{s^{N_t}(\boldsymbol{\mu}) - s_N^{N_t}(\boldsymbol{\mu})}. \tag{4.11}$$

As already stated in (3.5), the effectivities should be as close as possible to unity for sharpness, and ≥ 1 for rigor. We will now derive some results that state that the error bounds

introduced above indeed fulfill the requirements of rigor and sharpness [37]. If we choose $v = e(\boldsymbol{\mu})$ in (4.5) it follows with the Cauchy-Schwarz inequality and the definition of the coercivity constant (2.3) that

$$\alpha^{N_t}(\boldsymbol{\mu})\|e(\boldsymbol{\mu})\|_X^2 \leq a(e(\boldsymbol{\mu}),e(\boldsymbol{\mu});\boldsymbol{\mu}) \equiv \|e(\boldsymbol{\mu})\|_{\boldsymbol{\mu}}^2 = (\hat{e}(\boldsymbol{\mu}),e(\boldsymbol{\mu}))_X \leq \|\hat{e}(\boldsymbol{\mu})\|_X \|e(\boldsymbol{\mu})\|_X. \tag{4.12}$$

From inequalities in (4.12) together with the definition of the effectivity (4.8), we can conclude that $\eta_N^{\text{en}}(\boldsymbol{\mu}) \geq 1$, that means that our energy error bound is indeed a rigorous upper bound for the error measured in the energy norm - feasibility and safety are guaranteed. A similar procedure, but now with $v = \hat{e}(\boldsymbol{\mu})$ in (4.5) gives us, with the definition of the continuity constant (2.4) and again with the Cauchy-Schwarz inequality:

$$\|\hat{e}(\boldsymbol{\mu})\|_X^2 \leq \|\hat{e}(\boldsymbol{\mu})\|_{\boldsymbol{\mu}} \|e(\boldsymbol{\mu})\|_{\boldsymbol{\mu}}, \qquad \|\hat{e}(\boldsymbol{\mu})\|_{\boldsymbol{\mu}} \leq (\gamma^e(\boldsymbol{\mu}))^{\frac{1}{2}} \|\hat{e}(\boldsymbol{\mu})\|_X. \tag{4.13}$$

Now the definition of the effectivity (4.10) together with the inequalities (4.13) lead to the following result:

$$\begin{aligned} \Delta_N^{\text{en}}(\boldsymbol{\mu}) = (\alpha_{LB}^{N_t}(\boldsymbol{\mu}))^{-\frac{1}{2}} \|\hat{e}(\boldsymbol{\mu})\|_X &\leq (\gamma^e(\boldsymbol{\mu}))^{\frac{1}{2}} (\alpha_{LB}^{N_t}(\boldsymbol{\mu}))^{-\frac{1}{2}} \|e(\boldsymbol{\mu})\|_{\boldsymbol{\mu}} \\ \Rightarrow \eta_N^{\text{en}}(\boldsymbol{\mu}) &\leq \sqrt{\frac{\gamma^e(\boldsymbol{\mu})}{\alpha_{LB}^{N_t}(\boldsymbol{\mu})}}. \end{aligned} \tag{4.14}$$

This result states that the energy error bound overestimates the true error by at most $\sqrt{(\gamma^e(\boldsymbol{\mu})/\alpha_{LB}^{N_t}(\boldsymbol{\mu}))}$, independent of N, and hence is stable with respect to RB refinement. Stability with respect to FE refinements can be achieved if we can find a lower bound for the coercivity constant $\alpha_{LB}^{N_t}(\boldsymbol{\mu})$ which depends only on $\boldsymbol{\mu}$, or if $\alpha^{N_t}(\boldsymbol{\mu})/\alpha_{LB}^{N_t}(\boldsymbol{\mu})$ is bounded by a constant for most $\boldsymbol{\mu} \in \mathcal{D}$. The effectivity is then bounded by [49]

$$\eta_N^{\text{en}} \leq \sqrt{\frac{\gamma^e(\boldsymbol{\mu})}{\alpha_{LB}^{N_t}(\boldsymbol{\mu})}} \leq \sqrt{\frac{\alpha^{N_t}(\boldsymbol{\mu})}{\alpha_{LB}^{N_t}(\boldsymbol{\mu})}} \sqrt{\frac{\gamma^e(\boldsymbol{\mu})}{\alpha^e(\boldsymbol{\mu})}}, \quad \forall \boldsymbol{\mu} \in \mathcal{D}. \tag{4.15}$$

We will present the construction of such a lower bound for the coercivity constant in section 5. Similar results can be proven for the output error bound if we use equation (3.19), which states that $s^{N_t}(\boldsymbol{\mu}) - s_N^{N_t}(\boldsymbol{\mu}) = \|e(\boldsymbol{\mu})\|_{\boldsymbol{\mu}}^2$ and $\Delta_N^{\text{s}}(\boldsymbol{\mu}) = (\Delta_N^{\text{en}}(\boldsymbol{\mu}))^2$:

$$\eta_N^{\text{s}}(\boldsymbol{\mu}) = \frac{(\Delta_N^{\text{en}}(\boldsymbol{\mu}))^2}{\|e(\boldsymbol{\mu})\|_{\boldsymbol{\mu}}^2} = (\eta_N^{\text{en}}(\boldsymbol{\mu}))^2. \tag{4.16}$$

To sum up, for any $N = 1,\ldots,N_{\max}$, the effectivities satisfy

$$1 \leq \eta_N^{\text{en}}(\boldsymbol{\mu}) \leq \sqrt{\frac{\gamma^e(\boldsymbol{\mu})}{\alpha_{LB}^{N_t}(\boldsymbol{\mu})}}, \qquad 1 \leq \eta_N^{\text{s}}(\boldsymbol{\mu}) \leq \frac{\gamma^e(\boldsymbol{\mu})}{\alpha_{LB}^{N_t}(\boldsymbol{\mu})}, \qquad \forall \boldsymbol{\mu} \in \mathcal{D}. \tag{4.17}$$

4.3 Offline-Online Procedure

The error bounds developed in the previous section are only useful if they allow for an efficient offline-online computational procedure that leads to an online complexity independent of N_t. The offline-online decomposition presented in the following is mainly based on the dual norm of the residual. With the affine decomposition of $u_N^{N_t}(\boldsymbol{\mu})$ (2.5) and the expansion of $u_N^{N_t}(\boldsymbol{\mu})$ in the N basis functions (3.7), the residual can be expressed as

$$r(v;\boldsymbol{\mu}) = f(v) - a(u_N^{N_t}(\boldsymbol{\mu}),v;\boldsymbol{\mu}) = f(v) - \sum_{n=1}^{N} u_{Nn}^{N_t}(\boldsymbol{\mu}) \sum_{q=1}^{Q_a} \Theta^q(\boldsymbol{\mu}) a^q(\zeta_n^{N_t},v). \tag{4.18}$$

Together with (4.4) and linear superposition, this gives us

$$(\hat{e}(\boldsymbol{\mu}),v)_X = f(v) - \sum_{q=1}^{Q_a} \sum_{n=1}^{N} \Theta^q(\boldsymbol{\mu}) u_{Nn}^{N_t}(\boldsymbol{\mu}) a^q(\zeta_n^{N_t},v). \tag{4.19}$$

It then follows that we may write $\hat{e}(\boldsymbol{\mu}) \in X^{N_t}$ as

$$\hat{e}(\boldsymbol{\mu}) = \mathcal{F} + \sum_{q=1}^{Q_a} \sum_{n=1}^{N} \Theta^q(\boldsymbol{\mu}) u_{Nn}^{N_t}(\boldsymbol{\mu}) \mathcal{A}_n^q, \tag{4.20}$$

where $\mathcal{F} \in X^{N_t}$ and $\mathcal{A}_n^q \in X^{N_t}$ (called FE "pseudo"-solutions) satisfy

$$(\mathcal{F},v)_X = f(v), \quad \forall v \in X^{N_t}, \tag{4.21}$$

$$(\mathcal{A}_n^q,v)_X = -a^q(\zeta_n^{N_t},v), \quad \forall v \in X^{N_t}, 1 \le n \le N, 1 \le q \le Q_a. \tag{4.22}$$

We note that (4.21) and (4.22) are simple parameter-independent Poisson-like problems and thus can be solved once in the offline stage. It then follows that:

$$\begin{aligned} \|\hat{e}(\boldsymbol{\mu})\|_X^2 &= \left(\mathcal{F} + \sum_{q=1}^{Q_a} \sum_{n=1}^{N} \Theta^q(\boldsymbol{\mu}) u_{Nn}^{N_t}(\boldsymbol{\mu}) \mathcal{A}_n^q, \mathcal{F} + \sum_{q'=1}^{Q_a} \sum_{n'=1}^{N} \Theta^{q'}(\boldsymbol{\mu}) u_{Nn'}^{N_t}(\boldsymbol{\mu}) \mathcal{A}_{n'}^{q'} \right)_X \\ &= (\mathcal{F},\mathcal{F})_X + \sum_{q=1}^{Q_a} \sum_{n=1}^{N} \Theta^q(\boldsymbol{\mu}) u_{Nn}^{N_t}(\boldsymbol{\mu}) \left\{ 2(\mathcal{F},\mathcal{A}_n^q)_X + \sum_{q'=1}^{Q_a} \sum_{n'=1}^{N} \Theta^{q'}(\boldsymbol{\mu}) u_{Nn'}^{N_t}(\boldsymbol{\mu}) (\mathcal{A}_n^q,\mathcal{A}_{n'}^{q'})_X \right\}. \end{aligned} \tag{4.23}$$

This expression can be related to the requisite dual norm of the residual through (4.6). It is the sum of products of parameter-dependent known functions and parameter independent inner products, formed of more complicated but precomputable quantities. The offline-online decomposition is thus clear.

In the offline stage we first solve (4.21), (4.22) for the parameter-independent FE "pseudo"-solutions $\mathcal{F}$ and $\mathcal{A}_n^q, 1 \le n \le N_{\max}, 1 \le q \le Q_a$ and form/store the parameter-independent inner products $(\mathcal{F},\mathcal{F})_X$, $(\mathcal{F},\mathcal{A}_n^q)_X$, $(\mathcal{A}_n^q,\mathcal{A}_n^q)_X, 1 \le n \le N_{\max}, 1 \le q \le Q_a$. The offline operation count depends then on $N_{\max}$, Q_a and N_t.

In the online stage - performed for each new value of $\boldsymbol{\mu}$ - we simply evaluate the sum (4.23) in terms of the $\Theta^q(\boldsymbol{\mu}), 1 \le q \le Q_a$ and $u_{Nn}^{N_t}(\boldsymbol{\mu}), 1 \le n \le N$ (already computed for

the output evaluation) and the precalculated and stored (parameter-independent) $(\cdot,\cdot)_X$ inner products. The online operation count, and hence the marginal and asymptotic average cost, is only $\mathcal{O}(Q_a^2 N^2)$, and thus the crucial point - the independence of N_t - is again achieved. We further note that, unless Q_a is quite large, the online cost associated with the calculation of the residual dual norm and the online cost associated with the calculation of $s_N^{N_t}(\boldsymbol{\mu})$ are comparable. Again, the hierarchical properties of our reduced basis approximation spaces allow us to simply extract the necessary quantities for any $N \in \{1,\ldots,N_{\max}\}$ from the corresponding quantities for $N = N_{\max}$.

4.4 Upper and Lower Bounds for the Outputs

The output error estimators introduced in the previous sections for the compliant case can serve us to compute reliable upper and lower bounds $s_N^{N_t+}(\boldsymbol{\mu})$ and $s_N^{N_t-}(\boldsymbol{\mu})$ for the "truth" output $s^{N_t}(\boldsymbol{\mu})$ for each new value for $\boldsymbol{\mu}$ based on the RB output $s_N^{N_t}(\boldsymbol{\mu})$, such that

$$s_N^{N_t+}(\boldsymbol{\mu}) \geq s^{N_t}(\boldsymbol{\mu}) \geq s_N^{N_t-}(\boldsymbol{\mu}), \quad \forall \boldsymbol{\mu} \in \mathcal{D}, \forall N \in [1,\ldots,N_{\max}]. \tag{4.24}$$

We establish these limits as

$$s_N^{N_t-}(\boldsymbol{\mu}) = s_N^{N_t}(\boldsymbol{\mu}), \tag{4.25}$$

$$s_N^{N_t+}(\boldsymbol{\mu}) = s_N^{N_t}(\boldsymbol{\mu}) + \Delta_N^s(\boldsymbol{\mu}). \tag{4.26}$$

To demonstrate that equation (4.25) is indeed valid, we note that in the compliant case

$$\begin{aligned} s^{N_t}(\boldsymbol{\mu}) - s_N^{N_t}(\boldsymbol{\mu}) &= f(u^{N_t}(\boldsymbol{\mu}) - u_N^{N_t}(\boldsymbol{\mu})) = a(u^{N_t}(\boldsymbol{\mu}), u^{N_t}(\boldsymbol{\mu}) - u_N^{N_t}(\boldsymbol{\mu}); \boldsymbol{\mu}) \\ &= a(u^{N_t}(\boldsymbol{\mu}) - u_N^{N_t}(\boldsymbol{\mu}), u^{N_t}(\boldsymbol{\mu}) - u_N^{N_t}(\boldsymbol{\mu}); \boldsymbol{\mu}) \geq 0. \end{aligned} \tag{4.27}$$

This results of the definition of the symmetry of a, Galerkin orthogonality (3.21) and coercivity. This important result (which has also been stated in section 3.6.1) confirms that our reduced basis approximation is a lower bound for the FE solution. The validity of the upper bound (4.26) results directly from (4.17):

$$\eta_N^s(\boldsymbol{\mu}) \geq 1 \quad \Rightarrow \quad \Delta_N^s(\boldsymbol{\mu}) \geq s^{N_t}(\boldsymbol{\mu}) - s_N^{N_t}(\boldsymbol{\mu}) \Rightarrow \quad s_N^{N_t+}(\boldsymbol{\mu}) = s_N^{N_t}(\boldsymbol{\mu}) + \Delta_N^s(\boldsymbol{\mu}) \geq s^{N_t}(\boldsymbol{\mu}).$$

These upper and lower bounds for the underlying "truth" FE output play an important role for example in optimization problems. They assure that possible constraints are not only met for the reduced basis output, but also for the "truth" output. In many other applications this property has a great importance.

5 Coercivity Lower Bounds

We review the efficient computation of lower bounds for the coercivity constant (2.3) whose discrete version is a generalized eigenvalue problem. We will recall here the Successive Constraint Method (SCM) described in [13, 49]. This algorithm has been developed for the special requirements of the reduced basis method and thus features an efficient offline-online strategy which makes the online calculation complexity independent of N_t - a fundamental requisite.

5.1 Coercive Problems: The Successive Constraint Method

Even if we still consider a symmetric, continuous and coercive bilinear form a, which is affine in the parameter, the following results can be readily extended to non-symmetric operators [49] and general non-coercive operators [37]. We introduce an objective function $J^{\text{obj}}: \mathcal{D} \times \mathbb{R}^{Q_a} \to \mathbb{R}$ given by

$$J^{\text{obj}}(\boldsymbol{\mu}; y) = \sum_{q=1}^{Q_a} \Theta^q(\boldsymbol{\mu}) y_q, \quad \text{with } y = (y_1, \ldots, y_{Q_a}). \tag{5.1}$$

Next, the set $Y \in \mathbb{R}^{Q_a}$ is defined by

$$Y = \left\{ y \in \mathbb{R}^{Q_a} \,\middle|\, \exists\, w_y \in X^{N_t} \quad \text{s.t. } y_q = \frac{a^q(w_y, w_y)}{\|w_y\|_X^2}, \quad 1 \le q \le Q_a \right\}. \tag{5.2}$$

The affine parameter decomposition (2.5) allows us now to express our FE coercivity constant (defined in 2.3) as

$$\alpha^{N_t}(\boldsymbol{\mu}) = \inf_{y \in Y} J^{\text{obj}}(\boldsymbol{\mu}; y). \tag{5.3}$$

The next step is to introduce a "continuity constraint" box

$$B = \prod_{q=1}^{Q_a} \left[\inf_{w \in X^{N_t}} \frac{a^q(w,w)}{\|w\|_X^2}, \sup_{w \in X^{N_t}} \frac{a^q(w,w)}{\|w\|_X^2} \right] \tag{5.4}$$

which, from our continuity hypothesis, is bounded. The last ingredient is a "coercivity constraint" sample, $C_J = \{\boldsymbol{\mu}^1_{\text{SCM}} \in \mathcal{D}, \ldots, \boldsymbol{\mu}^J_{\text{SCM}} \in \mathcal{D}\}$; $C_J^{M,\boldsymbol{\mu}}$ denotes the subset of C_J with the $M (\ge 1)$ points closest (in the Euclidian norm) to a given $\boldsymbol{\mu} \in \mathcal{D}$. We make the convention $C_J^{M,\boldsymbol{\mu}} = C_J$ if $M > J$.

5.1.1 Lower Bound

Our strategy is to define a set $Y_{LB}(\boldsymbol{\mu}; C_J, M)$ which is relatively easy/cheap to compute and which can be used as surrogate for Y in (5.3). For given $C_J \in \mathcal{D}$ and $M \in \mathbb{N}$, this set must contain the original set Y, that means

$$Y \subset Y_{LB}(\boldsymbol{\mu}; C_J, M), \quad \forall \boldsymbol{\mu} \in \mathcal{D}. \tag{5.5}$$

If we choose

$$Y_{LB}(\boldsymbol{\mu}; C_J, M) \equiv \left\{ y \in \mathbb{R}^{Q_a} \,\middle|\, y \in B, \quad \sum_{q=1}^{Q_a} \Theta^q(\boldsymbol{\mu}') y_q \ge \alpha^{N_t}(\boldsymbol{\mu}'), \quad \forall \boldsymbol{\mu}' \in C_J^{M,\boldsymbol{\mu}} \right\} \tag{5.6}$$

as our "surrogate set", we can prove that (5.5) is indeed fulfilled. In fact, from the definition of Y (5.2) it follows that for any $y \in Y$, $\exists\, w_y \in X^{N_t}$ such that $y_q = \frac{a^q(w_y, w_y)}{\|w_y\|_X^2}, 1 \le q \le Q_a$. Then, since

$$\inf_{w \in X^{N_t}} \frac{a^q(w,w)}{\|w\|_X^2} \le \frac{a^q(w_y, w_y)}{\|w_y\|_X^2} \le \sup_{w \in X^{N_t}} \frac{a^q(w,w)}{\|w\|_X^2}, \tag{5.7}$$

and also

$$\sum_{q=1}^{Q_a} \Theta^q(\boldsymbol{\mu}) \frac{a^q(w_y, w_y)}{\|w_y\|_X^2} = \frac{a(w_y, w_y; \boldsymbol{\mu})}{\|w_y\|_X^2} \ge \alpha^{N_t}(\boldsymbol{\mu}), \quad \forall \boldsymbol{\mu} \in \mathcal{D}, \tag{5.8}$$

we can deduce that every member y of Y is also a member of $Y_{LB}^{N_t}(\boldsymbol{\mu};C_J,M)$, which concludes the proof. We can now define our lower bound as

$$\alpha_{LB}^{N_t}(\boldsymbol{\mu};C_J,M) = \min_{y\in Y_{LB}(\boldsymbol{\mu};C_J,M)} J^{\text{obj}}(\boldsymbol{\mu};y). \tag{5.9}$$

This definition is indeed a correct choice, as we can show with (5.5), that for given $C_J \subset \mathcal{D}$ and $M \in \mathbb{N}$

$$\alpha_{LB}^{N_t}(\boldsymbol{\mu}) = \min_{y\in Y_{LB(\boldsymbol{\mu};C_J,M)}} J^{\text{obj}}(\boldsymbol{\mu};y) \leq \min_{y\in Y} J^{\text{obj}}(\boldsymbol{\mu};y) = \alpha_{LB}^{N_t}(\boldsymbol{\mu}), \quad \forall \boldsymbol{\mu}\in\mathcal{D}.$$

This means that the necessary requirement for a lower bound, $\alpha_{LB}^{N_t}(\boldsymbol{\mu}) \leq \alpha^{N_t}(\boldsymbol{\mu})$, $\forall \boldsymbol{\mu}\in\mathcal{D}$, is fulfilled. The computation of our lower bound (5.9) is in fact a linear optimization problem (or Linear Program (LP)) [49]. It contains Q_a design variables and $2Q_a+M$ inequality constraints. It is important to note that again, this approach allows us to evaluate $\boldsymbol{\mu}\rightarrow\alpha_{LB}^{N_t}(\boldsymbol{\mu})$ with a computational cost independent of N_t, if B and the set $\{\alpha^{N_t}(\boldsymbol{\mu}')|\boldsymbol{\mu}'\in C_J\}$ are given. The (offline) computation of these quantities however is N_t-dependent. We will discuss the offline-online decomposition and computational costs in more detail in section 5.1.4.

5.1.2 Upper Bound

Although it is not directly necessary for our error bounds, we may also compute an upper bound for the coercivity constant. This will serve us for the efficient construction of a good coercivity constraint sample C_J. Similar to the approach for the lower bound, we introduce an "upper bound" set $Y_{UB}(\boldsymbol{\mu};C_J,M)\in\mathbb{R}^{Q_a}$ as

$$Y_{LB}(\boldsymbol{\mu};C_J,M) = \left\{ y^*(\boldsymbol{\mu}') \mid \boldsymbol{\mu}'\in C_J^{M,\boldsymbol{\mu}} \right\}, \tag{5.10}$$

where $y^*(\boldsymbol{\mu}) = \arg\inf_{y\in Y} J^{\text{obj}}(\boldsymbol{\mu};y)$. Our upper bound is then defined by

$$\alpha_{UB}^{N_t}(\boldsymbol{\mu};C_J,M) = \min_{y\in Y_{LB}(\boldsymbol{\mu};C_J,M)} J^{\text{obj}}(\boldsymbol{\mu};y).$$

As we can see directly from (5.10), $Y_{UB}(\boldsymbol{\mu};C_J,M)\subset Y$. It then follows that, for given $C_J, M\in\mathbb{N}$:, $\alpha_{UB}^{N_t}(\boldsymbol{\mu};C_J,M)\geq\alpha^{N_t}(\boldsymbol{\mu}),\forall\boldsymbol{\mu}\in\mathcal{D}$. That means our choice for $\alpha_{UB}^{N_t}(\boldsymbol{\mu})$ is indeed suited as upper bound for the coercivity constant. Again we can state that the operation count for the online evalutation $\boldsymbol{\mu}\rightarrow\alpha_{UB}^{N_t}(\boldsymbol{\mu})$ is independent of N_t (if the set $\{y^*(\boldsymbol{\mu}')|\boldsymbol{\mu}'\in C_J\}$ is already given).

5.1.3 Selection of C_J

The selection process for C_J will be based on a greedy algorithm somewhat similar to the greedy selection process for the basis functions described in section 3.5. We shall again introduce a "train" sample $\Xi_{\text{train,SCM}} = \{\boldsymbol{\mu}^1_{\text{train,SCM}},\dots,\boldsymbol{\mu}^{n_{\text{train,SCM}}}_{\text{train,SCM}}\}\subset\mathcal{D}$ of $n_{\text{train,SCM}}$ parameter

points and a tolerance $\epsilon_{\text{SCM}} \in [0,1]$ for the error in the lower bound prediction. We start with $J=1$ and $C_1 = \{\boldsymbol{\mu}_{\text{SCM}}\}$ chosen arbitrary. The greedy algorithm is then given by

$$\begin{aligned}
&\texttt{While} \quad \alpha_{\text{tol}}^J = \max_{\boldsymbol{\mu}\in\Xi_{\text{train,SCM}}} \left[\frac{\alpha_{UB}^{N_t}(\boldsymbol{\mu};C_J,M) - \alpha_{LB}^{N_t}(\boldsymbol{\mu};C_J,M)}{\alpha_{UB}^{N_t}(\boldsymbol{\mu};C_J,M)}\right] > \epsilon_{\text{SCM}}: \\
&\qquad \boldsymbol{\mu}_{\text{SCM}}^{J+1} = \arg\max_{\boldsymbol{\mu}\in\Xi_{\text{train,SCM}}} \left[\frac{\alpha_{UB}^{N_t}(\boldsymbol{\mu};C_J,M) - \alpha_{LB}^{N_t}(\boldsymbol{\mu};C_J,M)}{\alpha_{UB}^{N_t}(\boldsymbol{\mu};C_J,M)}\right]; \\
&\qquad C_{J+1} = C_J \cup \boldsymbol{\mu}_{\text{SCM}}^{J+1}; \quad J \leftarrow J+1; \\
&\quad \texttt{end.} \\
&\texttt{Set } J_{\max} = J
\end{aligned} \tag{5.11}$$

We choose $\alpha_{UB}(\boldsymbol{\mu};C_J,M)$ in the denominator of α_{tol}^J, as this value is strictly positive, contrary to $\alpha_{LB}(\boldsymbol{\mu};C_J,M)$ which may be negative or zero.

Indeed, the strategy is basically the same as in the greedy algorithm in section 3.5. In each iteration of the greedy procedure, we add to our "coercivity constraint" sample that point in $\mathcal{D}$ for which the current lower bound approximation is least accurate. The true error is thereby replaced by a (computationally cheaper) surrogate which makes it possible to perform a more efficient and more exhaustive search. Furthermore, it is important to note that our choice of stopping criterion allows us to bound

$$\begin{aligned}
\frac{\alpha^{N_t}(\boldsymbol{\mu})}{\alpha_{LB}^{N_t}(\boldsymbol{\mu};C_{J_{\max}},M)} &= \frac{\alpha^{N_t}(\boldsymbol{\mu})}{\alpha_{UB}^{N_t}(\boldsymbol{\mu};C_{J_{\max}},M)} \cdot \frac{\alpha_{UB}^{N_t}(\boldsymbol{\mu};C_{J_{\max}},M)}{\alpha_{LB}^{N_t}(\boldsymbol{\mu};C_{J_{\max}},M)} \\
&\leq \frac{\alpha^{N_t}(\boldsymbol{\mu})}{\alpha_{UB}^{N_t}(\boldsymbol{\mu};C_{J_{\max}})} \frac{1}{1-\epsilon_{\text{SCM}}} \leq \frac{1}{1-\epsilon_{\text{SCM}}}, \qquad \forall \boldsymbol{\mu} \in \Xi_{\text{train,SCM}}.
\end{aligned}$$

This result can be inserted in (4.15) to obtain the upper bounds for the effectivities which are now independent of N and N_t. Usually, we set $\epsilon_{\text{SCM}} = 0.75$, which is rather crude. Nevertheless this choice has relatively little detrimental effect on our error bounds.

5.1.4 Offline-Online Procedure

Finally, we precise the offline-online decomposition for the computation of the coercivity lower bounds and give an overview of the operation counts involved.

In the offline stage, we first have to build B and the set $\{\alpha^{N_t}(\boldsymbol{\mu}') | \boldsymbol{\mu}' \in C_{J_{\max}}\}$. This results in $2Q_a$ resp. $J_{\max}$ eigenproblems over X^{N_t}. Second, we have to subsequently form the set $\{y^*(\boldsymbol{\mu}') | \boldsymbol{\mu}' \in C_{J_{\max}}\}$ ($J_{\max} Q_a$ inner products over X^{N_t}). The last offline step is the solution of the $n_{\text{train,SCM}} J_{\max}$ linear optimization problems of "size" $2Q_a + M$ to perform the "arg max". The offline computational cost thus roughly scales as $\mathcal{O}(N_t \cdot (2Q_a + J_{\max})) + \mathcal{O}(N_t Q_a J_{\max}) + \mathcal{O}(n_{\text{train,SCM}} J_{\max} Q_a M)$. As already mentioned before, the offline computational costs of course depend on N_t, but N_t and $n_{\text{train,SCM}}$ do not occur as

a product in any of the terms - there is no term $\mathcal{O}(N_t n_{\text{train,SCM}})$. This means that we can choose both N_t and $n_{\text{train,SCM}}$ very large.

For each evaluation $\boldsymbol{\mu} \rightarrow \alpha_{LB}^{N_t}(\boldsymbol{\mu}; C_J, M)$ in the online stage, we first perform a sort of the $J_{\max}$ points in $C_{J_{\max}}$ to determine the set $C_{J_{\max}}^{M,\boldsymbol{\mu}}$. The operation count here is at most $\mathcal{O}(MJ_{\max})$. Then we must perform the $(M+1)Q_a$ evaluations $\boldsymbol{\mu}' \rightarrow \theta^q(\boldsymbol{\mu}'), 1 \leq q \leq Q_a$, which results in an operation count of $\mathcal{O}((M+1)Q_a)$. The last step is the extraction of the selected M members of the pre-computed set $\{\alpha^{N_t}(\boldsymbol{\mu}') | \boldsymbol{\mu}' \in C_J\}$ and the solution of the resulting linear optimization problem to obtain $\alpha_{LB}^{N_t}(\boldsymbol{\mu}; C_J, M)$. The fundamental point is again that the online evaluation count is independent of N_t and the rapid evaluation of the error bounds is supported by the SCM procedure.

6 Affine Geometric Parametric Variations

In the following, the fundamentals for affine geometric variations in the reduced basis context in two-dimensional domain will be presented. A more detailed introduction with many examples for different kinds of geometries can be found in [49].

6.1 Some preconditions

The RB recipe requires a parameter independent domain Ω as the snapshots we use for the construction of our basis functions have to be defined relative to the same spatial configuration. This difficulty can be resolved by interpreting Ω as parameter independent reference domain which is related to the parameter-dependent "actual" or "original" domain of interest $\Omega_o(\boldsymbol{\mu})$ via an affine mapping $T^{\text{aff}}(\boldsymbol{x}; \boldsymbol{\mu})$. We can then introduce a domain decomposition of $\Omega_o(\boldsymbol{\mu})$,

$$\Omega_o(\boldsymbol{\mu}) = \bigcup_{k=1}^{K_{\text{dom}}} \Omega_o^k(\boldsymbol{\mu}), \tag{6.1}$$

which consists of mutually nonoverlapping open subdomains $\Omega_o^k(\boldsymbol{\mu}), 1 \leq k \leq K_{\text{dom}}$, $\Omega_o^k(\boldsymbol{\mu}) \cap \Omega_o^{k'}(\boldsymbol{\mu}) = \emptyset$, $1 \leq k < k' \leq K_{\text{dom}}$. Our reference domain is then simply defined for a reference parameter value $\boldsymbol{\mu}_{\text{ref}} \in \mathcal{D}$ as $\Omega \equiv \Omega_o(\boldsymbol{\mu}_{\text{ref}})$; in the following we will identify $\Omega^k = \Omega_o^k(\boldsymbol{\mu}_{\text{ref}}), 1 \leq k \leq K_{\text{dom}}$ for brevity. The "K_{dom}" domain decomposition of Ω shall be denoted our "RB triangulation"; it will play an important role in the generation of our affine representation (2.5). The very fine N_t FE mesh will be a subtriangulation of the RB triangulation. Both the FE and RB approximations are defined over the reference domain. The choice of $\boldsymbol{\mu}_{\text{ref}}$ has an influence on the accuracy of the underlying FE approximation as it controls the distortion of the mesh for the actual domains. As mentioned before, the original domain (resp. the original subdomains) and the reference domain (resp. the reference subdomains) must be connectable via an affine mapping $T^{\text{aff}}(\cdot; \boldsymbol{\mu}) : \Omega^k \rightarrow \Omega_o^k(\boldsymbol{\mu}), 1 \leq k \leq K_{\text{dom}}$:

$$\Omega_o^k(\boldsymbol{\mu}) = T^{\text{aff},k}(\Omega^k; \boldsymbol{\mu}), \quad 1 \leq k \leq K_{\text{dom}}; \tag{6.2}$$

the affine mappings must be individually bijective and collectively continuous, that means they have to fulfill the following interface condition:

$$T^{\text{aff},k}(\boldsymbol{x};\boldsymbol{\mu}) = T^{\text{aff},k'}(\boldsymbol{x};\boldsymbol{\mu}), \quad \forall \boldsymbol{x} \in \Omega^k \cap \Omega^{k'}, \quad 1 \le k < k' \le K_{\text{dom}}. \tag{6.3}$$

For reasons of computational efficiency it is important to note that K_{dom} is defined with respect to the exact problem and therefore does not depend on N_t. The concrete affine transformations are then given for $1 \le k \le K_{\text{dom}}$, for any $\boldsymbol{\mu} \in \mathcal{D}$ and for any $\boldsymbol{x} \in \Omega^k$ as

$$T_i^{\text{aff},k}(\boldsymbol{x},\boldsymbol{\mu}) = C_i^{\text{aff},i}(\boldsymbol{\mu}) + \sum_{j=1}^{d} G_{ij}^{\text{aff},k}(\boldsymbol{\mu}) x_j, \quad 1 \le i \le d, \tag{6.4}$$

for given translation vectors $C^{\text{aff},k} : \mathcal{D} \to \mathbb{R}^d$ and linear transformation matrices $G^{\text{aff},i} : \mathcal{D} \to \mathbb{R}^{d \times d}$. The linear transformation matrices can effect rotation, scaling and/or shear and have to be invertible. The associated Jacobians can be defined as $J^{\text{aff},k}(\boldsymbol{\mu}) = |\det(G^{\text{aff},k}(\boldsymbol{\mu}))|$, $1 \le k \le K_{\text{dom}}$; for invertible mappings they are strictly positive. We note that the interface condition (6.3) allows us to interprete the set of local mappings as a global bijective piecewise affine transformation $T^{\text{aff}}(\cdot;\boldsymbol{\mu}) : \Omega \to \Omega_o(\boldsymbol{\mu})$. This global mapping is then given for any $\boldsymbol{\mu} \in \mathcal{D}$ by

$$T^{\text{aff}}(\boldsymbol{x};\boldsymbol{\mu}) = T^{\text{aff},k}(\boldsymbol{x};\boldsymbol{\mu}), \quad k = \min_{k' \in \{1,\ldots,K_{\text{dom}}\} | \boldsymbol{x} \in \Omega^{k'}} k'. \tag{6.5}$$

6.2 Affine Mappings for a Single Subdomain

Let us focus on the technology to define our affine mappings and present the basic building blocks of our RB triangulation that allow well-defined affine transformations. As for these purposes it is sufficient to concentrate on a single subdomain, we shall suppress the subdomain superscript for clarity of exposition. The matrices $C^{\text{aff}}(\boldsymbol{\mu}) \in \mathbb{R}^d$ and $G^{\text{aff}}(\boldsymbol{\mu}) \in \mathbb{R}^{d \times d}$ in (6.4) are now called "mapping coefficients".

We will now recall some of the properties of affine transformations in two dimensions. First, straight lines are mapped to straight lines, parallelism is preserved and parallel lines of equal length are also mapped on parallel lines of equal length. Consequently, a parallelogram is mapped to a parallelogram and hence a triangle maps to a triangle. Second, an affine transformation maps ellipses to ellipses. These features will be exploited in the following for the development of a domain decomposition technique that is suitable for the RB context. The affine mapping contains in the two-dimensional ($d = 2$) case $d(d+1) = 6$ degrees of freedom, the mapping coefficients. It is therefore sufficient, for any given $\boldsymbol{\mu} \in \mathcal{D}$, to consider the relationship between three non-colinear pre-image points in Ω, (z^1, z^2, z^3) and three parametrized image nodes in $\Omega_o(\boldsymbol{\mu})$, $(z_o^1(\boldsymbol{\mu}), z_o^2(\boldsymbol{\mu}), z_o^3(\boldsymbol{\mu}))$. Note that every point consists of two components $(z_1^i, z_2^i), 1 \le i \le 3$, resp. $(z_{o1}^i, z_{o2}^i), 1 \le i \le 3$, and therefore the application of (6.4) to these points constitutes a system of six independent equations to determine the six mapping coefficients:

$$z_{oi}^m(\boldsymbol{\mu}) = C_i^{\text{aff}}(\boldsymbol{\mu}) + \sum_{j=1}^{2} G_{ij}^{\text{aff}}(\boldsymbol{\mu}) z_j^m, \quad 1 \le i \le 2, \quad 1 \le m \le 3; \tag{6.6}$$

The assumption that the affine transformation is bijective thereby ensures that the image nodes are perforce also non-colinear (if the pre-image nodes are non-colinear) and hence the equations are perforce linear independent.

Our RB triangulation shall be built on (standard) triangles, elliptical triangles and general "curvy" triangles. They admit symbolic and numerical automation and are therefore the building blocks of choice in the rbMIT software package [44] that we use for the reduced basis computations in this work. This software, the techniques applied and its usage are briefly presented in section 9. The three basic building block types are discussed in detail below, with a special emphasys on elliptical triangles.

6.2.1 Standard Triangles

In the case of a standard triangle subdomain the three vertices of the triangle in the reference domain shall serve as pre-image nodes while the three vertices of the triangle in the actual ($\boldsymbol{\mu}$-dependent) domain shall serve as image nodes. In this case, our three points uniquely define not only the transformation but also the reference domain and parametrized domains. We recall that the pre-image nodes are obtained as the image nodes for a particlular value of the parameter $\boldsymbol{\mu}_{\text{ref}}$. We can then readily establish the system of six linear equations to determine the six unknown mapping coefficients. In this way, we can construct an affine transformation from any reference triangle in $\mathbb{R}^2$ onto any desired triangle in $\mathbb{R}^2$. We note that it is not mandatory to choose the vertices of the triangles as our nodes defining the transformation, other characteristic points e.g. the barycentric coordinates of the FE context are also possible.

6.2.2 Elliptical Triangles

The class of elliptical triangles covers a much greater range of possible geometries and their formulation is also necessary for the more general case dealing with curvy triangles. We can distinguish two different kinds of elliptic triangles: "inwards" and "outwards" triangles. Both types are depicted in Figure 2. In both cases, the elliptical triangle $\Omega_o(\boldsymbol{\mu})$ is defined by the three vertices $z_o^1(\boldsymbol{\mu}), z_o^2(\boldsymbol{\mu}), z_o^3(\boldsymbol{\mu})$, the two straight lines $\overline{z_o^1(\boldsymbol{\mu})z_o^2(\boldsymbol{\mu})}$ and $\overline{z_o^1(\boldsymbol{\mu})z_o^3(\boldsymbol{\mu})}$ as well as the elliptical arc $\overline{z_o^2(\boldsymbol{\mu})z_o^3(\boldsymbol{\mu})}^{\text{arc}}$.

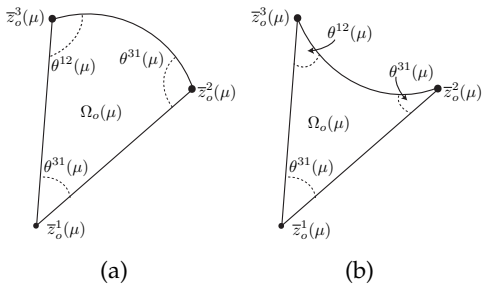

Figure 2: (a) "Inwards" elliptical triangle and (b) "outwards" elliptical triangle

We shall now precise the definition and description of the elliptical arc and explain the constraints that must be met by the location of the third point $z_o^1(\mu)$ to ensure "proper" triangles and a continuous and well-defined global mapping in the multidomain context.

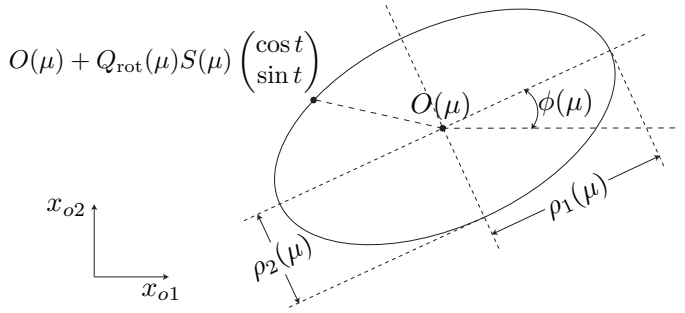

Figure 3: Definition of a point on a prescribed parametrized ellipse.

First, the description of the elliptical arc shall be derived from the definition of a parametrized ellipse as depicted in Figure 3. The ellipse is described implicitly by

$$(\boldsymbol{x}_o - O(\boldsymbol{\mu}))^T Q_{\mathrm{rot}}(\boldsymbol{\mu}) S^{-2}(\boldsymbol{\mu}) Q_{\mathrm{rot}}(\boldsymbol{\mu})^T (\boldsymbol{x}_o - O(\boldsymbol{\mu})) = 1. \tag{6.7}$$

A particular point on this ellipse is then given by

$$\boldsymbol{x}_o \equiv \begin{pmatrix} x_{o1} \\ x_{o2} \end{pmatrix} = O(\boldsymbol{\mu}) + Q_{\mathrm{rot}}(\boldsymbol{\mu}) S(\boldsymbol{\mu}) \begin{pmatrix} \cos t \\ \sin t \end{pmatrix} \tag{6.8}$$

for given $t \in \mathbb{R}$. As we can see in Figure 3, $O(\boldsymbol{\mu}) : D \to \mathbb{R}^2$ is the center of the ellipse, $\rho_1(\boldsymbol{\mu}) : D \to \mathbb{R}_+$ and $\rho_2 : D \to \mathbb{R}_+$ define the length of the semi-axes of the ellipse and $\phi(\boldsymbol{\mu}) : D \to \mathbb{R}$ is the angle of inclination. With these quantities, the scaling matrix $S(\boldsymbol{\mu})$ and the rotation matrix $Q_{\mathrm{rot}}(\boldsymbol{\mu})$ can be defined:

$$S(\boldsymbol{\mu}) \equiv \begin{pmatrix} \rho_1(\boldsymbol{\mu}) & 0 \\ 0 & \rho_2(\boldsymbol{\mu}) \end{pmatrix}, \qquad Q_{\mathrm{rot}}(\boldsymbol{\mu}) = \begin{pmatrix} \cos\phi(\boldsymbol{\mu}) & -\sin\phi(\boldsymbol{\mu}) \\ \sin\phi(\boldsymbol{\mu}) & \cos\phi(\boldsymbol{\mu}) \end{pmatrix}.$$

The description of the elliptical arc with these means is then as follows:

$$\overline{z_o^2(\boldsymbol{\mu}) z_o^3(\boldsymbol{\mu})}^{\mathrm{arc}} = \left\{ O(\boldsymbol{\mu}) + Q_{\mathrm{rot}}(\boldsymbol{\mu}) S(\boldsymbol{\mu}) \begin{pmatrix} \cos t \\ \sin t \end{pmatrix} \,\middle|\, t_2 \le t \le t_3 \right\}. \tag{6.9}$$

with $t_2 \in \mathbb{R}$ and $t_3 \in \mathbb{R}$ chosen such that the points $z_o^2(\boldsymbol{\mu})$ and $z_o^3(\boldsymbol{\mu})$ are given as the endpoints of the elliptical arc for $t = t_2$ and $t = t_3$:

$$z_o^m(\boldsymbol{\mu}) = O(\boldsymbol{\mu}) + Q_{\mathrm{rot}}(\boldsymbol{\mu}) S(\boldsymbol{\mu}) \begin{pmatrix} \cos t_m \\ \sin t_m \end{pmatrix}, \quad m = 2,3. \tag{6.10}$$

In addition, we have to make sure that $0 \le t_3 - t_2 < \pi$. It remains to specify the location of the third point $z_o^1(\boldsymbol{\mu})$. For elliptical triangles, this location has to be chosen in a way that ensures that the affine transformation generates the desired elliptical arc (6.9). First, this ensures a continuous global mapping; second, to obtain well-defined elliptical triangles

and consequently a well defined domain in the multidomain context, several internal angle conditions have to be met by the choice for $z_o^1(\boldsymbol{\mu})$: $0<\theta^*<\pi, \forall\theta^*\in\{\theta^{12},\theta^{23},\theta^{31}\}$. The first requirement can be fulfilled by the expression of the three corner points as

$$z_o^m(\boldsymbol{\mu}) = O(\boldsymbol{\mu}) + \omega_m Q_{\text{rot}}(\boldsymbol{\mu}) S(\boldsymbol{\mu}) \begin{pmatrix} \cos t_m \\ \sin t_m \end{pmatrix}, \quad 1 \le m \le 3, \tag{6.11}$$

for given $\omega_1 = \omega \in \mathbb{R}$, $\omega_2 = \omega_3 = 1$ and $t_1 \in [t_2, t_3]$. Consequently, the pre-image points are given as

$$z_o^m(\boldsymbol{\mu}_{\text{ref}}) = O(\boldsymbol{\mu}_{\text{ref}}) + \omega_m Q_{\text{rot}}(\boldsymbol{\mu}_{\text{ref}}) S(\boldsymbol{\mu}_{\text{ref}}) \begin{pmatrix} \cos t_m \\ \sin t_m \end{pmatrix}, \quad 1 \le m \le 3. \tag{6.12}$$

From these representations we can identify our affine mapping as

$$\begin{aligned} z_o^m(\boldsymbol{\mu}) = C^{\text{aff}}(\boldsymbol{\mu}) + G^{\text{aff}}(\boldsymbol{\mu}) z^m = (O(\boldsymbol{\mu}) - Q_{\text{rot}}(\boldsymbol{\mu}) S(\boldsymbol{\mu}) S(\boldsymbol{\mu}_{\text{ref}})^{-1} Q_{\text{rot}}(\boldsymbol{\mu}_{\text{ref}})^T O(\boldsymbol{\mu}_{\text{ref}})) \\ + (Q_{\text{rot}}(\boldsymbol{\mu}) S(\boldsymbol{\mu}) S(\boldsymbol{\mu}_{\text{ref}})^{-1} Q_{\text{rot}}(\boldsymbol{\mu}_{\text{ref}})^T) z^m. \end{aligned} \tag{6.13}$$

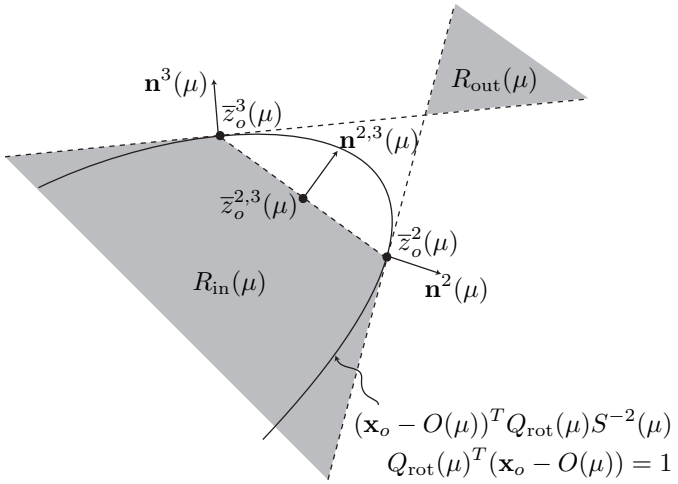

Figure 4: Regions in which $z_o^1(\boldsymbol{\mu})$ must reside for an elliptical triangle in the inwards case ($R_{\text{in}}(\boldsymbol{\mu})$) and the outwards case ($R_{\text{out}}(\boldsymbol{\mu})$).

The second requirement - the internal angle conditions - is illustrated in Figure 4 [49]. In the inwards case, a necessary and sufficient condition to ensure the internal angle conditions $0< \theta^* <\pi$, $\forall\ \theta^*\in\{\theta^{12}, \theta^{23}, \theta^{31}\}$ is given for an inwards elliptical triangle by $z_o^1(\boldsymbol{\mu}) \in R_{\text{in}}(\boldsymbol{\mu})$, where

$$\begin{aligned} R_{in}(\boldsymbol{\mu}) = \{ z_o^1(\boldsymbol{\mu}) \in \mathbb{R}^2 | (z_o^1(\boldsymbol{\mu}) - z_o^2(\boldsymbol{\mu}))^T \boldsymbol{n}^2(\boldsymbol{\mu}) < 0, \\ (z_o^1(\boldsymbol{\mu}) - z_o^3(\boldsymbol{\mu})))^T \boldsymbol{n}^3(\boldsymbol{\mu}) < 0, (z_o^1(\boldsymbol{\mu}) - z_o^{2,3}(\boldsymbol{\mu}))^T \boldsymbol{n}^{2,3}(\boldsymbol{\mu}) < 0 \}, \end{aligned} \tag{6.14}$$

and for the outwards elliptical triangle by $z_o^1(\boldsymbol{\mu}) \in R_{\text{out}}(\boldsymbol{\mu})$, where

$$R_{out}(\boldsymbol{\mu}) = \{ z_o^1(\boldsymbol{\mu}) \in \mathbb{R}^2 | (z_o^1(\boldsymbol{\mu}) - z_o^2(\boldsymbol{\mu}))^T \boldsymbol{n}^2(\boldsymbol{\mu}) > 0, (z_o^1(\boldsymbol{\mu}) - z_o^3(\boldsymbol{\mu}))^T \boldsymbol{n}^3(\boldsymbol{\mu}) > 0 \}. \tag{6.15}$$

Here $\boldsymbol{n}^2(\boldsymbol{\mu})$ and $\boldsymbol{n}^3(\boldsymbol{\mu})$ are the outwards-facing normals to the ellipse at $\boldsymbol{z}^2(\boldsymbol{\mu})$ and $\boldsymbol{z}^3(\boldsymbol{\mu})$ respectively, $\boldsymbol{z}_o^{2,3}(\boldsymbol{\mu}) = \frac{1}{2}(\boldsymbol{z}_o^2(\boldsymbol{\mu}) + \boldsymbol{z}_o^3(\boldsymbol{\mu}))$ and $\boldsymbol{n}^{2,3}(\boldsymbol{\mu})$ is the "outwards-facing" normal to the line segment $\overline{\boldsymbol{z}_o^2(\boldsymbol{\mu})\boldsymbol{z}_o^3(\boldsymbol{\mu})}$ at $\boldsymbol{z}_o^{2,3}(\boldsymbol{\mu})$.

We note here that for elliptical triangles it is possible to derive explicit conditions on ω such that the internal angle conditions (6.14) and (6.15) are satisfied, for details see [49]. These conditions are independent of $\boldsymbol{\mu}$. An important feature of the elliptical triangles is that they are consistent under refinement, that means that if we split an elliptical triangle for which the internal angle conditions (6.14) and (6.15) are fulfilled, the resulting two elliptical triangles also satisfy the internal angle conditions. To enlarge the possible range of geometries even more, the elliptical triangles are extended to "curvy" triangles. This is done by replacing $(\cos t, \sin t)^T$ in (6.9) with a general parametrization $(g_1(t), g_2(t))^T$.

6.2.3 Piecewise-Affine Mappings for Multiple Subdomains

To treat more complex geometries, it is necessary to allow our domain to be built of several (standard, elliptical or curvy) triangles, dealing with a piecewise affine mapping based on this domain decomposition. We can thus consider geometrical domains and regions for which the boundary and internal interfaces can be represented either by straight edges or by elliptical triangles as presented in the numerical tests.

The multi-domain mapping process is then performed in three steps. First, the RB triangulation is generated on the reference domain Ω together with the associated reference subdomains. The RB triangulation has to be compatible with the mapping continuity condition (6.3) and all elliptical and curvy subtriangles have to be well-defined and to fulfilll the internal angle conditions (6.14) and (6.15). The procedure applied to generate this RB triangulation is implemented in the rbMIT software package [44]. In the second step, the necessary parameter-dependent affine mappings for each subdomain are constructed, as described in the previous section. In the last step we have to translate the parametric mappings obtained for each subdomain into PDE coefficients.

6.3 Bilinear Forms for Affine Geometric Parametric Variations

In this section we deal with the use of the affine mappings derived in the previous sections to get an affine representation (2.5) of the problem (which has a parameter-dependent geometry) on a parameter-independent reference geometry. We will first address the transformation of the formulation on the original domain to the formulation on the reference domain and then explain how the affine representation can be derived.
If we consider a problem analogue to (2.1) with a parameter-dependent domain $\Omega_o(\boldsymbol{\mu})$ which realizes the affine geometry precondition as described in the previous section, this problem can be written in general form as: given $\boldsymbol{\mu} \in \mathcal{D}$, evaluate

$$s_o^e(\boldsymbol{\mu}) = l_o(u_o^e(\boldsymbol{\mu})), \tag{6.16}$$

where $u_o^e(\boldsymbol{\mu}) \in X_o^e(\boldsymbol{\mu})$ satisfies

$$a_o(u_o^e(\boldsymbol{\mu}), v; \boldsymbol{\mu}) = f_o(v), \quad \forall v \in X_o^e(\boldsymbol{\mu}). \tag{6.17}$$

For simplicity we assume that we have homogeneous Dirichlet boundary conditions over the entire boundary, which corresponds to $X_o^e(\boldsymbol{\mu}) = H_0^1(\Omega_o(\boldsymbol{\mu}))$. A sufficient condition on $a_o(\cdot,\cdot;\boldsymbol{\mu}) : H^1(\Omega_o(\boldsymbol{\mu})) \times H^1(\Omega_o(\boldsymbol{\mu})) \rightarrow \mathbb{R}$ that ensures an affine expansion of the bilinear form (if the affine geometry precondition is fulfilled) is fulfilled if we have

$$a_o(w,v;\boldsymbol{\mu}) = \sum_{k=1}^{K_{\text{dom}}} \int_{\Omega_o^k(\boldsymbol{\mu})} \begin{bmatrix} \frac{\partial w}{\partial x_{o1}} & \frac{\partial w}{\partial x_{o2}} \end{bmatrix} K_{o,k}(\boldsymbol{\mu}) \begin{bmatrix} \frac{\partial v}{\partial x_{o1}} \\ \frac{\partial v}{\partial x_{o2}} \end{bmatrix}. \tag{6.18}$$

The matrices $K_{o,k} : \mathcal{D} \rightarrow \mathbb{R}^{2\times 2}, 1 \leq k \leq K_{\text{dom}}$ are in the symmetric case symmetric positive definite matrices. A similar requirement may be posed on $f_o(\cdot;\boldsymbol{\mu}) : H^1(\Omega_o(\boldsymbol{\mu})) \rightarrow \mathbb{R}$: we require that it can be expressed as

$$f_o(v;\boldsymbol{\mu}) = \sum_{k=1}^{K_{\text{dom}}} \int_{\Omega_o^k(\boldsymbol{\mu})} F_{o,k}(\boldsymbol{\mu}) v, \tag{6.19}$$

with $F_{o,k} : \mathcal{D} \rightarrow \mathbb{R}$, $1 \leq k \leq K_{\text{dom}}$. To transform this formulation on the reference domain to recover (2.1), we first identify $s^e(\boldsymbol{\mu}) = s_o^e(\boldsymbol{\mu}) \circ T^{\text{aff}}(\cdot;\boldsymbol{\mu})$ and $u^e(\boldsymbol{\mu}) = u_o^e(\boldsymbol{\mu}) \circ T^{\text{aff}}(\cdot;\boldsymbol{\mu})$. We then recall that

$$\frac{\partial}{\partial x_{oi}} = \frac{\partial x_j}{\partial x_{oi}} \frac{\partial}{\partial x_j} = (G^{\text{aff},k}(\boldsymbol{\mu}))_{1i}^{-1} \frac{\partial}{\partial x_1} + (G^{\text{aff},k}(\boldsymbol{\mu}))_{2i}^{-1} \frac{\partial}{\partial x_2} \quad i = 1,2, \tag{6.20}$$

in $\Omega_o^k(\boldsymbol{\mu})$ and $d\Omega_o^k(\boldsymbol{\mu}) = J^{\text{aff},k}(\boldsymbol{\mu}) d\Omega$. It then follows that the transformed bilinear form a can be expressed as

$$a(w,v;\boldsymbol{\mu}) = \sum_{k=1}^{K_{\text{dom}}} \int_{\Omega_k} \begin{bmatrix} \frac{\partial w}{\partial x_1} & \frac{\partial w}{\partial x_2} \end{bmatrix} K^k(\boldsymbol{\mu}) \begin{bmatrix} \frac{\partial v}{\partial x_1} \\ \frac{\partial v}{\partial x_2} \end{bmatrix}. \tag{6.21}$$

The $K^k : \mathcal{D} \rightarrow \mathbb{R}^{2\times 2}$ are given by

$$K^k(\boldsymbol{\mu}) = J^{\text{aff},k}(\boldsymbol{\mu}) G^k(\boldsymbol{\mu}) K_{o,k}(\boldsymbol{\mu}) (G^k(\boldsymbol{\mu}))^T,, 1 \leq k \leq K_{\text{dom}}, \tag{6.22}$$

while the $G^k : \mathcal{D} \rightarrow \mathbb{R}^{2\times 2}$ are given by

$$G^k(\boldsymbol{\mu}) = G^{\text{aff},k}(\boldsymbol{\mu})^{-1}, \quad 1 \leq k \leq K_{\text{dom}}.$$

The transformed linear form can be expressed similarly as

$$f(v;\boldsymbol{\mu}) = \sum_{k=1}^{K_{\text{dom}}} \int_{\Omega_k} F^k(\boldsymbol{\mu}) v,$$

where the $F^k : \mathcal{D} \rightarrow \mathbb{R}$ are given by

$$F^k(\boldsymbol{\mu}) = J^{\text{aff},k}(\boldsymbol{\mu}) F_{o,k}(\boldsymbol{\mu}), \quad 1 \leq k \leq K_{\text{dom}}.$$

In general, the $K^k(\boldsymbol{\mu})$ and $F^k(\boldsymbol{\mu})$ will be different for each subdomain Ω^k. The affine formulation (6.21) can then be derived by simply expanding this expression (in terms of the subdomains Ω^k and the different entries of $K_{ij}^k, 1 \leq i,j \leq 2, 1 \leq k \leq K_{\text{dom}}$). This results in

$$a(w,v;\boldsymbol{\mu}) = K_{11}^1(\boldsymbol{\mu}) \int_{\Omega^1} \frac{\partial w}{\partial x_1} \frac{\partial v}{\partial x_1} + K_{12}^1(\boldsymbol{\mu}) \int_{\Omega^1} \frac{\partial w}{\partial x_1} \frac{\partial v}{\partial x_2} + \cdots \tag{6.23}$$

The affine representation is now clear: for each term in (6.23) the (parameter-independent) integral represents $a^q(w,v)$, while the (parameter-dependent) prefactor represents $\Theta^q(\boldsymbol{\mu})$. The linear form f admits a similar treatment. The affine representation obtained by this process contains at most $Q_a = 3K_{\text{dom}}$ terms. In some special cases the number of nonzero terms in (6.23) is even reduced to $Q_a = 2K_{\text{dom}}$, like dealing with potential flows (without mixed derivatives in the Laplacian). In other situations, many terms can be economized if linear dependent entries are assembled together. Another possibility to reduce the number of terms Q_a is an intelligent choice of user-provided initial control points and edges for the RB triangulation. This can help to exploit symmetry effects and isolate geometric variation. We will come back to this issue in the practical part of this work.

7 Potential flows

We now consider the RB approximation and error bounds together with the affine geometry decomposition applied to potential flows which can be considered as one of the simplest two- or three-dimensional flow models describing laminar non-viscous and irrotational flows [5, 36, 51]. This case is of interest in the RB methodology development because we are going to consider outputs and error bounds related with the gradient of the state solution and not just related with the solution itself.
We will first precise the definition and properties of potential flows. We will then reformulate the necessary equations in order to obtain a problem equivalent to (2.1). As the special structure of potential flows allows us to solve a scalar equation for the so-called potential function ϕ: instead of a vectorial system for the velocity components and the pressure, we also develop a new set of special a posteriori error bounds for velocity and pressure based on the original error bounds for the scalar variable whose gradient gives the irrotational velocity fields:

$$\boldsymbol{u} = -\nabla\phi,$$

where $\boldsymbol{u} = (u_1, u_2)^T$ is the velocity and its components in x_1 and x_2 direction. Together with the continuity equation $\nabla \cdot \boldsymbol{u} = 0$, we obtain the governing Laplace equation for the potential:

$$-\Delta\phi = 0 \quad \text{in } \Omega_o(\boldsymbol{\mu}). \tag{7.1}$$

The pressure p at an arbitrary point in the domain $\Omega_o(\boldsymbol{\mu})$ can then subsequently be obtained by Bernoulli's equation:

$$p + \frac{1}{2}\rho|\boldsymbol{u}|^2 = p_{\text{in}} + \frac{1}{2}\rho|\boldsymbol{u}_{\text{in}}|^2, \quad \text{in } \Omega_o(\boldsymbol{\mu}),$$

and the pressure coefficient c_p can be defined as

$$c_p = \frac{p - p_{\text{in}}}{\frac{1}{2}\rho|\boldsymbol{u}_{\text{in}}|^2} = 1 - \left(\frac{|\boldsymbol{u}|^2}{|\boldsymbol{u}_{\text{in}}|^2}\right),$$

where p_{in} is the pressure of the undisturbed flow on the inflow boundary and $\boldsymbol{u}_{\text{in}}$ is the velocity vector of the undisturbed flow on the inflow boundary. Gravity effects are not included in this formulation, but could easily be added to the equation. Furthermore, a time dependency could be introduced in the pressure calculation by using a time dependent formulation of Bernoulli's equation, see e.g. [51]. Boundary conditions are given by homogeneous Neumann conditions

$$\frac{\partial \phi}{\partial n} = 0 \quad \text{on } \Gamma_{\text{w}}(\boldsymbol{\mu}) \tag{7.2}$$

to describe non-penetration on walls $\Gamma_{\text{w}}(\boldsymbol{\mu})$, inhomogeneous Neumann conditions

$$\frac{\partial \phi}{\partial \mathbf{n}} = \phi_{\text{in}} \quad \text{on } \Gamma_{\text{in}}(\boldsymbol{\mu}) \tag{7.3}$$

where $\phi_{\text{in}} = \mathbf{u}_{\text{in}} \cdot \mathbf{n}$ in order to impose the velocity $\mathbf{u}_{\text{in}}$ on the inflow boundary $\Gamma_{\text{in}}(\boldsymbol{\mu})$ and by (homogeneous or inhomogeneous) Dirichlet conditions

$$\phi = \phi_{\text{ref}} \quad \text{on } \Gamma_{\text{out}}(\boldsymbol{\mu}) \tag{7.4}$$

to prescribe the level of the potential, for example on the outflow boundary $\Gamma_{\text{out}}(\boldsymbol{\mu})$.

The weak formulation of the governing equations on the original domain $\Omega_o(\boldsymbol{\mu})$ can be found by standard integration by parts and reads as follows: find $\phi \in X^e \equiv H^1_{0,\Gamma_{out}}$ s.t.

$$a(\phi, v; \boldsymbol{\mu}) = f(v; \boldsymbol{\mu}) \quad \forall v \in X^e, \tag{7.5}$$

with

$$a(\phi, v; \boldsymbol{\mu}) = \int_{\Omega_o(\boldsymbol{\mu})} \nabla \phi \cdot \nabla v, \qquad f(v; \boldsymbol{\mu}) = \int_{\Gamma_{\text{in}}(\boldsymbol{\mu})} \phi_{\text{in}} v - \int_{\Omega_o(\boldsymbol{\mu})} \nabla R\phi_{\text{ref}} \cdot \nabla v, \tag{7.6}$$

where $R\phi_{\text{ref}} \in H^1(\Omega)$ is a lift function s.t. $R\phi_{\text{ref}}|_{\Gamma_{out}} = \phi_{\text{ref}}$. From the formulation (7.5) on the parameter dependent domain $\Omega_o(\boldsymbol{\mu})$, the formulation on the reference domain Ω can be derived with the methods introduced in section 6. The main steps are the affine decomposition of the original domain, the identification of the affine mappings and in the end the "translation" of the affine mapping coefficients to the formulation on the reference domain (2.1).

8 Error Bounds for Velocity and Pressure

The a posteriori error bounds developed in section 4 can be used to bound the error in the solution for the scalar potential function. To get an error bound for the error in velocity and pressure, we introduce some new considerations. This development allows to consider error bounds depending directly on the gradient of the state solution, enriching the variety of certified outputs we may consider.
We start with a given finite element triangulation of the domain $(\mathcal{T}_{N_t})$ with triangles T_{N_t}. The kinetic energy computed on a triangle T_{N_t} can then be represented by

$$K_{N_t}^{T_{N_t}} = \frac{1}{T_{N_t}} \int_{T_{N_t}} |\nabla \phi^{N_t}|^2 \quad \text{in } T_{N_t};$$

the potential function ϕ can be expected to be smooth enough to give $\nabla\phi \in C^0(\Omega)$ and $\nabla\phi$ can be interpreted pointwise; we may assume that $\phi \in C^1(\Omega)$, while $\phi^{N_t} \in X^{N_t}$ is the field solution of the FE "truth" approximation (2.2). The RB solution $\phi_N^{N_t} \in W_N^{N_t} \subset X^{N_t}$ then fulfills $a(\phi_N^{N_t}, v) = l(v)$, $\forall v \in W_N^{N_t}$. For simplicity, we omit the $\boldsymbol{\mu}$-dependency of the bilinear/linear forms and the error bounds in this section. Recall that the error between the reduced basis solution and the FE approximation $e_N^{N_t}$ is defined as $e_N^{N_t} = \phi^{N_t} - \phi_N^{N_t}$. With Δ_N^{en} being our usual energy error bound (4.8), we note that

$$a(e_N^{N_t}, e_N^{N_t}) = \int_\Omega |\nabla e_N^{N_t}|^2 \le (\Delta_N^{\text{en}})^2, \tag{8.1}$$

follows from the inequalities in (4.12). The RB approximation of $K_{N_t}^{T_{N_t}}$ is given as

$$K_N^{T_{N_t}} = \frac{1}{T_{N_t}} \int_{T_{N_t}} |\nabla \phi_N^{N_t}|^2 \quad \text{in } T_{N_t}. \tag{8.2}$$

We next introduce

$$I_N^{N_t} \equiv \left(\int_\Omega |\nabla \phi_N^{N_t}|^2 \right)^{1/2}. \tag{8.3}$$

Our aim is now to develop an error bound for the kinetic energy $K_N^{T_{N_t}}$ on T_{N_t}. On a single triangle, we note that

$$\begin{aligned} K_{N_t}^{T_{N_t}} - K_N^{T_{N_t}} &= \left| \frac{1}{T_{N_t}} \int_{T_{N_t}} |\nabla \phi^{N_t}|^2 - |\nabla \phi_N^{N_t}|^2 \right| = \frac{1}{T_{N_t}} \int_{T_{N_t}} \nabla(\phi^{N_t} - \phi_N^{N_t}) \cdot \nabla(\phi^{N_t} + \phi_N^{N_t}) \\ &= \frac{1}{T_{N_t}} \int_{T_{N_t}} \left(\nabla(\phi^{N_t} - \phi_N^{N_t}) \cdot \nabla(\phi^{N_t} - \phi_N^{N_t}) + 2\nabla(\phi^{N_t} - \phi_N^{N_t}) \cdot \nabla \phi_N^{N_t} \right) \\ &\le \frac{1}{T_{N_t}} \left(\int_{T_{N_t}} |\nabla(e_N^{N_t})|^2 + 2\left(\int_{T_{N_t}} |\nabla(e_N^{N_t})|^2 \right)^{1/2} \left(\int_{T_{N_t}} |\nabla \phi_N^{N_t}|^2 \right)^{1/2} \right). \end{aligned} \tag{8.4}$$

Hence all over the domain we compute the following quantity, giving the error on kinetic energy weighted with the area of each triangle of the mesh:

$$\begin{aligned} &\sum_{T_{N_t} \in \mathcal{T}_{N_t}} |T_{N_t}| |K_{N_t}^{T_{N_t}} - K_N^{T_{N_t}}| \\ &\le \sum_{T_{N_t} \in \mathcal{T}_{N_t}} \int_{T_{N_t}} \nabla(\phi^{N_t} - \phi_N^{N_t}) \cdot \nabla(\phi^{N_t} - \phi_N^{N_t}) + 2 \sum_{T_{N_t} \in \mathcal{T}_{N_t}} \int_{T_{N_t}} \nabla(\phi^{N_t} - \phi_N^{N_t}) \cdot \nabla \phi_N^{N_t} \\ &\le \sum_{T_{N_t} \in \mathcal{T}_{N_t}} \int_{T_{N_t}} |\nabla(e_N^{N_t})|^2 + 2 \sum_{T_{N_t} \in \mathcal{T}_{N_t}} \left(\int_{T_{N_t}} |\nabla(e_N^{N_t})|^2 \right)^{1/2} \left(\int_{T_{N_t}} |\nabla \phi_N^{N_t}|^2 \right)^{1/2} \\ &\le \int_\Omega |\nabla(e_N^{N_t})|^2 + \frac{1}{\sigma} \sum_{T_{N_t} \in \mathcal{T}_{N_t}} \int_{T_{N_t}} |\nabla(e_N^{N_t})|^2 + \sigma \sum_{T_{N_t} \in \mathcal{T}_{N_t}} \int_{T_{N_t}} |\nabla \phi_N^{N_t}|^2 \\ &\le (1 + \frac{1}{\sigma})(\Delta_N^{\text{en}})^2 + \sigma (I_N^{N_t})^2 \quad \le \quad (\Delta_N^{\text{en}})^2 + 2 I_N^{N_t} \Delta_N^{\text{en}} \equiv \Delta_N^K. \end{aligned} \tag{8.5}$$

by using the Young inequality and choosing, in particular, $\sigma = \sigma_{opt} = \Delta_N^{\text{en}} / I_N^{N_t}$. Thus Δ_N^K is a $L^1(\Omega)$ error bound for the RB prediction for the velocity squared ($|\nabla \phi_N^{N_t}|^2$). An error bound for the pressure can be obtained using (8.5) and Bernoulli's equation. If we define

$$p_{N_t}^{T_{N_t}} = \frac{1}{T_{N_t}} \int_{T_{N_t}} (B_{\text{in}} - \frac{\rho}{2} |\nabla \phi^{N_t}|^2), \qquad p_N^{T_{N_t}} = \frac{1}{T_{N_t}} \int_{T_{N_t}} (B_{\text{in}} - \frac{\rho}{2} |\nabla \phi_N^{N_t}|^2),$$

where $B_{\text{in}} \equiv p_{\text{in}} + \frac{\rho}{2} |\boldsymbol{u}_{\text{in}}|^2$ is given, the error bound for the pressure, as before, follows directly as

$$\sum_{T_{N_t} \in \mathcal{T}_{N_t}} |T_{N_T}| |p_{N_t}^{T_{N_t}} - p_N^{T_{N_t}}| \leq \frac{\rho}{2} \Delta_N^K \equiv \Delta_N^p.$$

8.1 Pointwise error bounds

We introduce also error bounds for pointwise calculations of velocity and pressure. Let us consider a point x_o as an internal point of the mesh triangle T_{Nto}. With ∇_o we indicate a discrete gradient computed on T_{Nto} and since we are using P_1 finite elements the gradient of the solution (ϕ) is constant over each triangle T_{Nto} and so the velocity $V_{No}(x_o)$ and pressure $p_{No}(x_o)$ given by

$$V_{No}(x_o) = \frac{1}{|T_{Nto}|} \int_{T_{Nto}} \nabla_o \phi_{No}, \qquad p_{No}(x_o) = 1 - \frac{1}{|T_{Nto}|} \int_{T_{Nto}} |\nabla_o \phi_{No}|^2.$$

We now develop an error bound for the pointwise squared velocity $|(\nabla \phi_{No})^2 - (\nabla \phi_o)^2|$. By indicating with pedix h the quantities related with FE solution, we note that

$$\begin{aligned}
|\mathcal{K}_h^{T_h} - \mathcal{K}_N^{T_h}| &= \left| \frac{1}{T_h} \int_{T_h} |\nabla \phi_h|^2 - |\nabla \phi_N|^2 \right| = \frac{1}{T_h} \int_{T_h} \nabla(\phi_h - \phi_N) \cdot \nabla(\phi_h + \phi_N) \\
&= \frac{1}{T_h} \int_{T_h} \nabla(\phi_h - \phi_N) \cdot \nabla(\phi_h - \phi_N) + 2\nabla(\phi_h - \phi_N) \cdot \nabla \phi_N \\
&\leq \frac{1}{T_h} \left(\int_{T_h} |\nabla \varepsilon_{h,N}|^2 + 2 \left(\int_{T_h} |\nabla \varepsilon_{h,N}|^2 \right)^{1/2} \left(\int_{T_h} |\nabla \phi_N|^2 \right)^{1/2} \right).
\end{aligned}$$

Hence

$$\begin{aligned}
|T_{Nto}| |(\nabla \phi_{No})^2 - (\nabla \phi_o)^2| &\leq \sum_{T_{Nt} \in \mathcal{T}_{Nt}} |T_{Nt}| |K_{N_t}^{T_{Nt}} - K_N^{T_{Nt}}| \\
&\leq \sum_{T_{Nt} \in \mathcal{T}_{Nt}} \int_{T_{Nt}} |\nabla e_N^{Nt}|^2 + \sum_{T_{Nt} \in \mathcal{T}_{Nt}} 2 \left(\int_{T_{nt}} |\nabla e_N^{Nt}|^2 \right)^{1/2} \left(\int_{T_{Nt}} |\nabla \phi_N|^2 \right)^{1/2} \\
&\leq \sum_{T_{Nt} \in \mathcal{T}_{nt}} \int_{\Omega} |\nabla e_N^{Nt}|^2 + \frac{1}{\sigma} \sum_{T_{nt} \in \mathcal{T}_{Nt}} \int_{T_{Nt}} |\nabla e_N^{Nt}|^2 + \sigma \sum_{T_{Nt} \in \mathcal{T}_{Nt}} \int_{T_{Nt}} |\nabla \phi_N|^2 \\
&\leq (1 + \frac{1}{\sigma}) (\Delta_N^{en})^2 + \sigma I_N^2 \leq (\Delta_N^{en})^2 + 2 I_N^2 \Delta_N^{en} \equiv \Delta_N^K,
\end{aligned}$$

choosing $\sigma = \sigma_{opt} = \Delta_N^{en} / I_N$ so that

$$|(\nabla \phi_{No})^2 - (\nabla \phi_o)^2| \leq \frac{1}{|T_{Nto}|} ((\Delta_N^{en})^2 + 2 I_N^2 \Delta_N^{en}) \equiv \frac{1}{|T_{Nto}|} \Delta_N^K$$

and

$$|p_{No} - p_o| \leq \frac{1}{|T_{Nto}|}\Delta_N^p.$$

We thus see that $\frac{1}{|T_{Nto}|}\Delta_N^K$ is essentially a $L^1(\Omega)$ error bound on the RB prediction for the pointwise velocity squared ($|\nabla\phi|^2$) and $\frac{1}{|T_{Nto}|}\Delta_N^p$ is essentially a $L^1(\Omega)$ error bound on the RB prediction for pointwise pressure.

9 Software, Geometries and Flow Models

For all computations, the rbMIT software [44] has been used. This library is designed for the solution of affine linear elliptic PDEs with the reduced basis method and is fully implemented in MATLAB. A documentation for rbMIT software is available in [12,37].

The software is based on an affine decomposition of the parametrized domain geometry into the three basic building blocks presented in section 6.2: standard triangles, elliptical triangles and more general curvy triangles. The geometry has been provided by a set of points (can be parameter dependent) and edges describing different regions. The edges can be either straight edges or parameter dependent curved lines, which have to be formulated as

$$\begin{pmatrix} x_{o1} \\ x_{o2} \end{pmatrix} = \begin{pmatrix} O_1(\boldsymbol{\mu}) \\ O_2(\boldsymbol{\mu}) \end{pmatrix} + \begin{pmatrix} \cos\phi(\boldsymbol{\mu}) & -\sin\phi(\boldsymbol{\mu}) \\ \sin\phi(\boldsymbol{\mu}) & \cos\phi(\boldsymbol{\mu}) \end{pmatrix} \begin{pmatrix} \rho_1(\boldsymbol{\mu}) & 0 \\ 0 & \rho_2(\boldsymbol{\mu}) \end{pmatrix} \begin{pmatrix} g_1(t) \\ g_2(t) \end{pmatrix}, \qquad (9.1)$$

for $t \in [t_1, t_2]$. Each edge has to be either convex or concave. This corresponds to the definition of our curvy triangles in section 6.2. If we choose $g_1(t) = \cos t$ and $g_2(t) = \sin t$, we obtain the definition of an elliptical arc fulfilling the affine geometry precondition.

The software first performs the three main steps described in section 6.2.3. We recall that the aim is to construct a domain decomposition (6.1) of the reference geometry Ω (defined by the user inputs) compatible with the interface condition (6.3). In addition, all elliptical and curvy triangles have to satisfy the consistency/continuity condition (6.11) and the internal angle conditions (6.14) and (6.15).
The software first focuses on all elliptical and curvy edges making part of the domain. For each elliptical or curvy arc, an elliptical, resp. curvy, triangle is introduced according to the definitions of section 6.2. In the case of internal interfaces, two triangles are needed. For each new triangle, an additional interior control point is added to the set of initial control points. If a triangle does not fulfilll the internal angle conditions or the interface condition, this triangle is split by the software into two triangles. This process is repeated until all introduced elliptical and curvy triangles are well-defined and consistent with the internal angle and interface conditions and the curved geometry is represented properly. After that, the algorithm fills the remainder of the domain with standard triangles by a Delaunay triangulation [49].

The parametrization of the curved geometry is unfortunately not arbitrary. The determination of the third point of an elliptical or a curvy triangle requires that the origin $(O_1(\boldsymbol{\mu}), O_2(\boldsymbol{\mu}))^T$ of the curve in the form (9.1) must not lie on the segment of the curve.

In addition, there is another possibility to control the domain decomposition process by defining additional initial control points and edges that are not necessary for the specification of the geometry. As illustrated with several examples in [49], a good choice of the control points can reduce the number of affine terms Q_a by enforcing a domain decomposition which results in many parametrically similar subdomains.

In the last steps, the parameter-dependent affine mappings for each subdomain are constructed and then translated into the PDE coefficients, as described in section 6.3. Finally, the FE system matrices and vectors have to be assembled (in the affine formulation (2.5)) and stored. In addition to the geometry and the problem to be solved, we have to specify the parameter range $\mathcal{D}$, the reference parameter $\boldsymbol{\mu}_{\text{ref}}$ and the value for $\overline{\boldsymbol{\mu}}$ in the X-norm definition. The parameter range has important implications on the performance of the RB method, since *(i)* a bigger parameter range will require more basis functions; *(ii)* the geometry should be well-defined for all $\boldsymbol{\mu} \in \mathcal{D}$; *(iii)* also the domain decomposition must not become singular for any $\boldsymbol{\mu} \in \mathcal{D}$. Here is a short overview of the subsequent steps performed by the software in the offline and online phase:

1. In the offline stage the greedy "train" sample $\Xi_{\text{train,SCM}}$ is built and the SCM algorithm is performed to compute the lower bounds for the coercivity constants for all members $\boldsymbol{\mu} \in \Xi_{\text{train,SCM}}$. After that, the reduced basis space is generated by the greedy algorithm and stored for the online stage.

2. In the online stage, the solution and output for a particular parameter value $\boldsymbol{\mu}$ are computed. For the computation of the solution, we can either prescribe a value for the desired accuracy or the number of basis functions. Then the lower bound for the coercivity constant $\alpha_{LB}^{N_t}(\boldsymbol{\mu}; C_J, M)$ is computed in order to calculate the a posteriori error bound (4.8) for the field variable. Finally, the field variable is used to compute the output (or outputs).

The computations, provided in this work as examples, have been done for three geometric configurations dealing with different problems: a Venturi channel, a curved bend and a basin. The following sections are devoted to the description of these problems.

10 A Venturi Channel

Flows in ducts, channels, and pipelines are of great interest in fluid mechanics applications especially when flows can be studied in a parametrized geometrical configuration. This first example considers a 2D potential flow into a Venturi channel and it can be seen as an example for the design of a parametrized fluidic device (which can be considered also as an element of a more complex modular fluidic system and by adopting a more complex fluid model). We illustrate the calculation of pressure and velocity by the Bernoulli Theorem and the curvy geometry parametrization. Velocity and pressure are influenced by the channel/constriction configuration (i.e. height and length of the throat and radius of curvature of the connection). The fluid velocity must increase through the

constriction to satisfy the equation of continuity, while its pressure must decrease due to conservation of energy. The gain in kinetic energy is supplied by a drop in pressure or a pressure gradient force. Gravitational effects or other force fields could be applied.

The limiting case of the Venturi effect is choked flow, in which a constriction in a pipe or channel limits the total flow rate through the channel because the pressure cannot drop below zero in the constriction. Choked flow is used to control the delivery rate of water and other fluids through valves. Examples of the Venturi effect are everywhere: in the capillaries of the human circulatory system; in large cities where wind is forced between buildings; in inspirators that mix air and flammable gas in burners; in atomizers and nozzles.

10.1 Problem Description

We consider the physical domain $\Omega_o(\boldsymbol{\mu})$ shown in Figure 5. Here $\mathbf{x} = (\mathbf{x_1}, \mathbf{x_2})$ denotes a point in $\Omega_o(\boldsymbol{\mu})$, non-dimensionalized with respect to height of the inlet $\widetilde{L}$. Note that a tilde $\tilde{}$ denotes dimensional quantities, and the absence of a tilde signals a non-dimensional quantity. We identify in Figure 5 the domain Ω_1, representing the Venturi channel (inlet, connection, throat, connection, oulet).

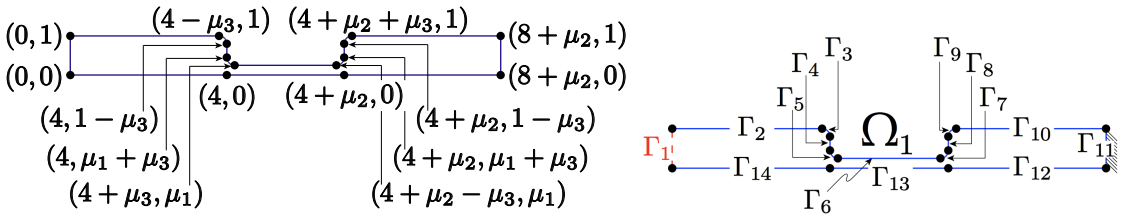

Figure 5: parametrized Geometry (left) and domain boundaries (right).

In this example the boundary segments Γ_3, Γ_5, Γ_7, Γ_9 are curved (all other boundary segments and internal interfaces are straight lines). The segment Γ_3 is given by the parametrization

$$\begin{bmatrix} x_1 \\ x_2 \end{bmatrix} = \underbrace{\begin{bmatrix} 4-\mu_3 \\ 1-\mu_3 \end{bmatrix}}_{O^1(\boldsymbol{\mu})} + \underbrace{\begin{bmatrix} 1 & 0 \\ 0 & 1 \end{bmatrix}}_{Q^1(\boldsymbol{\mu})} \underbrace{\begin{bmatrix} \mu_3 & 0 \\ 0 & \mu_3 \end{bmatrix}}_{S^1(\boldsymbol{\mu})} \begin{bmatrix} \cos(\pi t) \\ \sin(\pi t) \end{bmatrix},$$

where $t \in [0, 1/2]$. The segment Γ_5 is given by the parametrization

$$\begin{bmatrix} x_1 \\ x_2 \end{bmatrix} = \underbrace{\begin{bmatrix} 4+\mu_3 \\ \mu_1+\mu_3 \end{bmatrix}}_{O^2(\boldsymbol{\mu})} + \underbrace{\begin{bmatrix} 1 & 0 \\ 0 & 1 \end{bmatrix}}_{Q^2(\boldsymbol{\mu})} \underbrace{\begin{bmatrix} \mu_3 & 0 \\ 0 & \mu_3 \end{bmatrix}}_{S^2(\boldsymbol{\mu})} \begin{bmatrix} \cos(\pi t) \\ \sin(\pi t) \end{bmatrix},$$

where $t \in [1, 3/2]$. The segment Γ_7 is given by the parametrization

$$\begin{bmatrix} x_1 \\ x_2 \end{bmatrix} = \underbrace{\begin{bmatrix} 4+\mu_2-\mu_3 \\ \mu_1+\mu_3 \end{bmatrix}}_{O^3(\boldsymbol{\mu})} + \underbrace{\begin{bmatrix} 1 & 0 \\ 0 & 1 \end{bmatrix}}_{Q^3(\boldsymbol{\mu})} \underbrace{\begin{bmatrix} \mu_3 & 0 \\ 0 & \mu_3 \end{bmatrix}}_{S^3(\boldsymbol{\mu})} \begin{bmatrix} \cos(\pi t) \\ \sin(\pi t) \end{bmatrix},$$

where $t \in [3/2,2]$. The segment Γ_9 is given by the parametrization

$$\begin{bmatrix} x_1 \\ x_2 \end{bmatrix} = \underbrace{\begin{bmatrix} 4+\mu_2+\mu_3 \\ 1-\mu_3 \end{bmatrix}}_{O^4(\boldsymbol{\mu})} + \underbrace{\begin{bmatrix} 1 & 0 \\ 0 & 1 \end{bmatrix}}_{Q^4(\boldsymbol{\mu})} \underbrace{\begin{bmatrix} \mu_3 & 0 \\ 0 & \mu_3 \end{bmatrix}}_{S^4(\boldsymbol{\mu})} \begin{bmatrix} \cos(\pi t) \\ \sin(\pi t) \end{bmatrix},$$

where $t \in [1/2,1]$. The Venturi element could be integrated into a more complex modular system. We consider here $P = 3$ parameters. Here μ_1, μ_2, μ_3 are geometry parameters defined in Figure 5; μ_1 is the height of the throat (i.e., the central narrow part of the Venturi channel), μ_2 is the length of the narrow part of the channel, and μ_3 is the radius used to smooth the connections between the inlet (and the outlet) with the central throat. The parameter domain is given by $\mathcal{D} = [0.25,0.5] \times [2,4] \times [0.1,0.2]$. We show in Figure 5 the boundaries of the domain, on which we impose the following boundary conditions:

- homogeneous Dirichlet condition $\phi(\boldsymbol{\mu}) = 0$ on boundary Γ_{11};
- non-homogeneous Neumann condition $\frac{\partial \phi}{\partial \mathbf{n}} = 1$ on boundary Γ_1 (i.e., imposition of the velocity at the inlet);
- homogeneous Neumann conditions $\frac{\partial \phi}{\partial \mathbf{n}} = 0$ (i.e., zero normal velocity) on the other boundaries.

For this problem the output of interest is provided by the visualization of velocity field (by streamlines) and/or pressure contour field. The error bounds are computed on the pressure and on the velocity.
This problem is then modeled by the P_1 finite element (FE) discretization over the triangulation (represented in red) shown in Figure 6; the FE space contains $N_t = 3137$ degrees of freedom. FE approximation is typically too slow for man query and/or real time applications, and we hence approximate the FE prediction for the output and field variable by the reduced basis (RB) method.

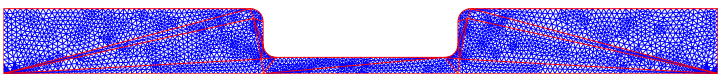

Figure 6: Finite Element Mesh

Figures 7 and 8 report some representative solutions for selected values of parameters and also an indication of the computed error bounds on velocity and recovered pressure.

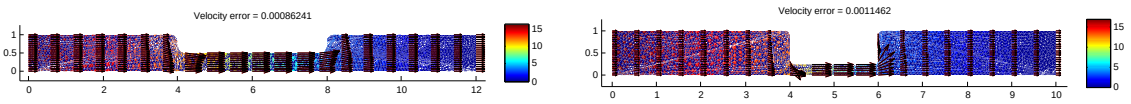

Figure 7: Representative solutions for potential and velocity (with error bounds) for $\mu = [0.25,2,0.1]$ and $\mu = [0.5,4,0.2]$.

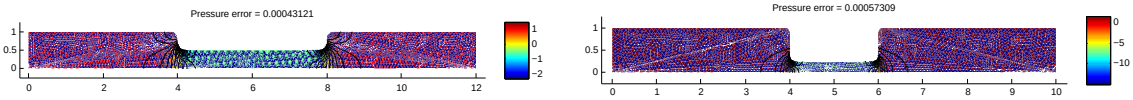

Figure 8: Representative solutions for pressure (with error bounds) for $\mu = [0.25,2,0.1]$ and $\mu = [0.5,4,0.2]$.

10.2 Numerical results

For this problem, with $P = 3$ parameters, we can visualize in Figure 9 the sample $S_{N_{\max}}$ obtained by application of the (energy version of the) greedy algorithm of Section 3.5 for Ξ_{train} a log-uniform random sample of size $n_{\text{train}} = 3000$. Clearly, the point distribution is very far from tensor-product in form: there is some clustering near the boundaries of the parameter domain, however the interior of the domain is very sparsely populated. We also note that the sample $S_{N_{\max}}$ reflects the particular problem of interest, as would be expected from the "adaptive" greedy procedure: the densest clustering of points is near regions of $\mathcal{D}$ in which the parametric sensitivity is largest. We also plot in Figure 9 the SCM lower and upper bounds for the coercivity constant, while in Figure 10 the quantity $\max_{\mu \in \Xi_{\text{train}}} \left(\Delta_N^{\text{en}}(\mu) / ||\phi_N^{N_t}(\mu)||_\mu \right)$ for the Lagrange RB approximations associated with the sample of Figure 9. We observe very rapid, exponential convergence.

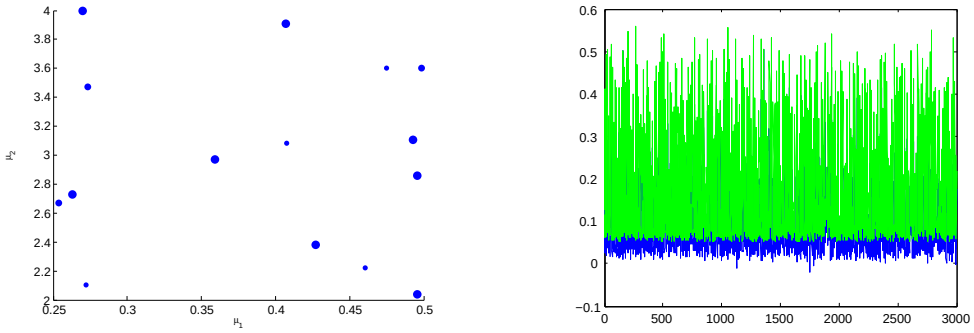

Figure 9: Venturi channel example. Left: greedy sample $S_{N_{\max}}$; note the value of μ_3 $(0.1 \le \mu_3 \le 0.2)$ is proportional to the radius of the circle. Right: upper and lower bounds for the coercivity constant, here Ξ_{train} is a log-uniform random sample of size $n_{\text{train}} = 3000$: $\alpha_{\text{UB}}^{N_t}(\mu)$ (upper curve, solid) and $\alpha_{\text{LB}}^{N_t}(\mu)$ (lower curve, dotted) as a function of $\mu' \in \Xi_{\text{train,SCM}}$ after $J_{\max} = 14$ iterations of the SCM greedy algorithm; here the abscissa represents the index of the point $\mu_{\text{train,SCM}}^k$ in $\Xi_{\text{train,SCM}}$.

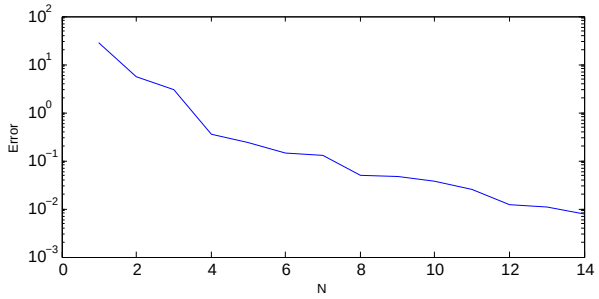

Figure 10: Venturi channel example: $\max_{\boldsymbol{\mu}\in\Xi_{\text{train}}}\left(\Delta_N^{\text{en}}(\boldsymbol{\mu})/||\phi_N^{N_t}(\boldsymbol{\mu})||_{\boldsymbol{\mu}}\right)$ as a function of N for the Lagrange RB approximations associated with the sample of Figure 9; here Ξ_{train} is a log-uniform random sample of size $n_{\text{train}} = 3000$.

11 Circular bend

In this second example we look at a potential flow into a bend with a parametrization on the internal and the external radius. Velocity and pressure are influenced by the bend configuration (i.e., angle and radius of curvature). The major points are the curved streamlines, the pressure gradient induced by the curvature, and the classical irrotational flow field associated with zero vorticity. Also gravitational effects or other force fields could be applied.

11.1 Problem Description

We consider the physical domain $\Omega_o(\boldsymbol{\mu})$ shown in Figure 11. Here $\mathbf{x} = (\mathbf{x_1}, \mathbf{x_2})$ denotes a point in $\Omega(\boldsymbol{\mu})$, non-dimensionalized with respect to a unit radius $\widetilde{R}$ (note that a tilde˜

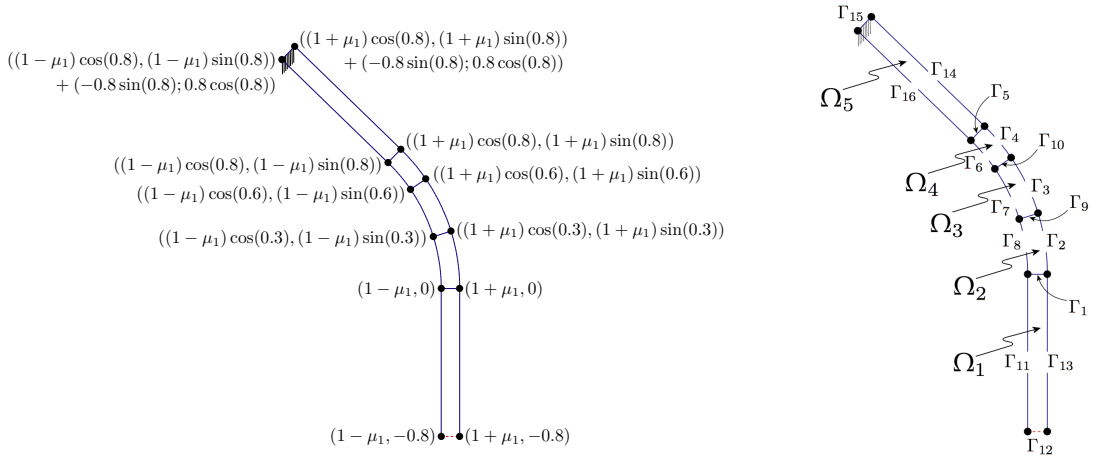

Figure 11: parametrized Geometry (left) and domain boundaries (right).

denotes dimensional quantities). We identify in Figure 11 the subdomains Ω_1,Ω_2,...,Ω_5, describing a bend for a given internal and external radius and an angle. The geometrical configuration studied in this problem is quite complex to be parametrized dealing with two curved walls at a small distance. In this problem the boundary segments Γ_2, Γ_3, Γ_4, Γ_6, Γ_7, and Γ_8 are curved (all other boundary segments and internal interfaces are straight lines). The segments Γ_6, Γ_7, and Γ_8 are given by the parametrization

$$\begin{bmatrix} x_1 \\ x_2 \end{bmatrix} = \underbrace{\begin{bmatrix} 0 \\ 0 \end{bmatrix}}_{O^1(\boldsymbol{\mu})} + \underbrace{\begin{bmatrix} 1 & 0 \\ 0 & 1 \end{bmatrix}}_{Q^1(\boldsymbol{\mu})} \underbrace{\begin{bmatrix} 1-\mu_1 & 0 \\ 0 & 1-\mu_1 \end{bmatrix}}_{S^1(\boldsymbol{\mu})} \begin{bmatrix} \cos(t) \\ \sin(t) \end{bmatrix},$$

where for Γ_6, $t \in [3/5,4/5]$, for Γ_7, $t \in [3/10,3/5]$, and for Γ_8, $t \in [0,3/10]$. The segments Γ_2, Γ_3, and Γ_4 are given by the parametrization

$$\begin{bmatrix} x_1 \\ x_2 \end{bmatrix} = \underbrace{\begin{bmatrix} 0 \\ 0 \end{bmatrix}}_{O^2(\boldsymbol{\mu})} + \underbrace{\begin{bmatrix} 1 & 0 \\ 0 & 1 \end{bmatrix}}_{Q^2(\boldsymbol{\mu})} \underbrace{\begin{bmatrix} 1+\mu_1 & 0 \\ 0 & 1+\mu_1 \end{bmatrix}}_{S^2(\boldsymbol{\mu})} \begin{bmatrix} \cos(t) \\ \sin(t) \end{bmatrix},$$

where for Γ_2, $t \in [0,3/10]$, for Γ_3, $t \in [3/10,3/5]$, and for Γ_4, $t \in [3/5,4/5]$. These curvy boundaries describe the walls of the bend, straight lines are representing the inlet and the outlet. The bend element could be integrated into a more complex modular system.

We consider here only $P = 1$ parameter: here μ_1 is the semi-width of the bend, so that internal radius is $1-\mu_1$ and the external one is $1+\mu_1$ (considering a unit radius as reference length $\widetilde{R}$); the angle (measured in radiant) between the inlet and the outlet is given, and its vertex is the origin of the concentric circles whose portions describes the curvy walls. The outflow/inflow straight zone is parametrized considering a length of $4\max(\mu_1)$. The parameter domain is given by $\mathcal{D} = [0.05,0.2]$.

We have also to impose interface and boundary conditions. We show in Figure 11 the boundaries of the domain. On boundary Γ_{15} we impose homogeneous Dirichlet conditions $\phi(\boldsymbol{\mu}) = 0$, while on boundaries Γ_2, Γ_3, Γ_4, Γ_6, Γ_7, Γ_8, Γ_{11}, Γ_{13}, Γ_{14}, and Γ_{16} we impose homogeneous Neumann conditions, $\frac{\partial \phi}{\partial \mathbf{n}} = 0$. In addition we impose non-homogeneous Neumann condition, $\frac{\partial \phi}{\partial \mathbf{n}} = 1$ at the inflow Γ_{12} (i.e., imposed inflow velocity). Also for this problem the output of interest is provided by the visualization of velocity field (by streamlines) and/or pressure contour field. The error bound is computed on the pressure.

This problem is then modeled by a P_1 finite element (FE) discretization whose space contains $\mathcal{N}_t = 7765$ degrees of freedom. FE approximation may be typically too slow for many query and real time applications, and we hence approximate the FE prediction for the output and field variable by the reduced basis (RB) method.

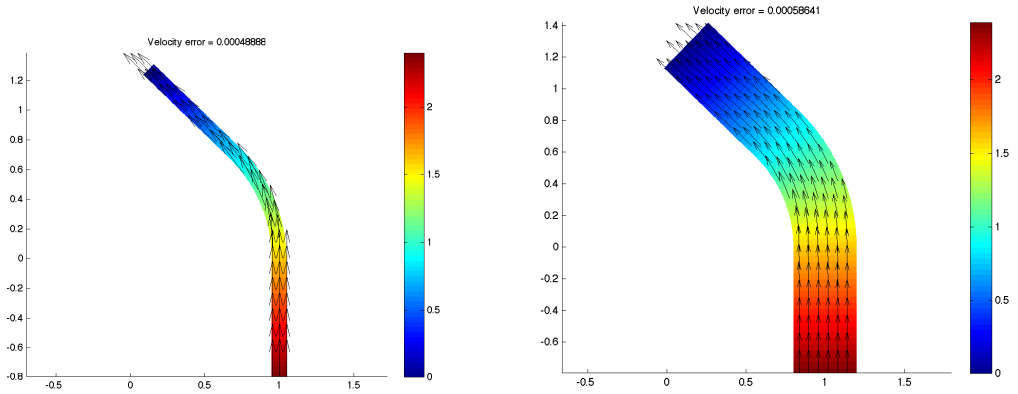

Figure 12: Representative solutions for potential and velocity (with error bounds) for $\mu = [0.05]$ and $\mu = [0.2]$.

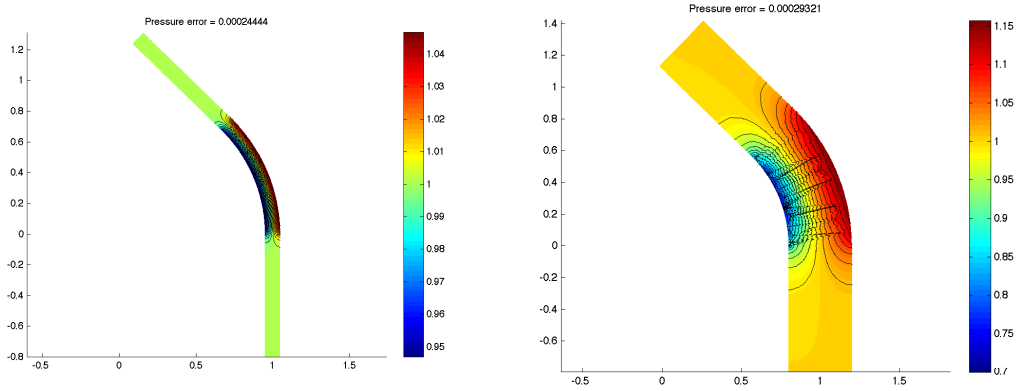

Figure 13: Representative solutions for pressure (with error bounds) for $\mu = [0.05]$ and $\mu = [0.2]$.

11.2 Numerical results

For this problem, considering one parameter $(P = 1)$, we can now build the sample $S_{N_{\max}} = [0.12, 0.06, 0.17]$ obtained by application of the (energy norm version of the) greedy algorithm of Section 3.5 for Ξ_{train} a log-uniform random sample of size $n_{\text{train}} = 1000$. We plot in Figure 14 $\max_{\mu \in \Xi \text{train}} \left(\Delta_N^{\text{en}}(\mu) / ||\phi_N^{N_t}(\mu)||_\mu \right)$ for the Lagrange RB approximations associated with the sample $S_{N_{\max}}$: we observe very rapid, exponential convergence and just 3 basis functions have been selected and used (this explains the linear plot).

12 Added mass

In this last example we provide a simple model to compute the added mass of a parametrized rectangular body in order to get added mass calculations not yet available in

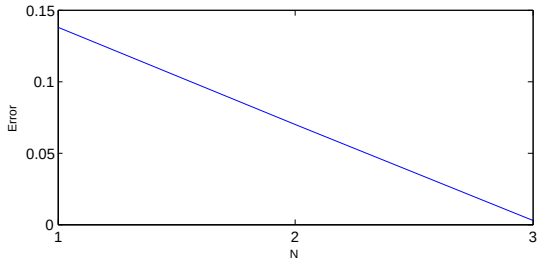

Figure 14: Circular bend example: $\max_{\boldsymbol{\mu}\in\Xi_{\text{train}}}\left(\Delta_N^{\text{en}}(\boldsymbol{\mu})/||\phi_N^{N_t}(\boldsymbol{\mu})||_{\boldsymbol{\mu}}\right)$ as a function of N for the Lagrange RB approximations associated with the sample $S_{N_{\max}}=[0.12,0.06,0.17]$; here Ξ_{train} is a log-uniform random sample of size $n_{\text{train}}=1000$.

the literature. This is a simple hydrodynamics problem. Its applications are well known and important not only in marine hydrodynamics and relatedly in naval architecture and ocean engineering (including oil drilling platforms), but also in more general fields studying floating and buoyancy effects. We consider here a simplified body floating into inviscid and incompressible flows using a potential flow model.

In fluid mechanics, added mass is the inertia added to a system because an accelerating or decelerating body must move some volume of surrounding fluid as it moves through it, since the object and fluid cannot occupy the same physical space simultaneously. For simplicity this can be modeled as some volume of fluid moving with the object, though in reality "all" the fluid will be accelerated, to various degrees. All bodies accelerating in a fluid will be affected by added mass, but since the added mass is dependent on the density of the fluid, the effect is often neglected for dense bodies falling in much less dense fluids. For situations where the fluid density is comparable to, or even greater than, the density of the body, the added mass can often be greater than the mass of the body and neglecting it can introduce significant errors into a calculation. See for example [25].

12.1 Problem Description

We consider the physical domain $\Omega_o(\boldsymbol{\mu})$ shown in Figure 15. We identify in Figure 15 the subdomains Ω_1 and Ω_2, which will serve to define the geometry or introduce inhomogeneous physical properties. The domain represents an outer box containing a rectangular body.

We consider here $P=3$ parameters. Here μ_1, μ_2, μ_3 are geometry parameters defined in Figure 15: μ_1 is the semi-width (basis) of the rectangular body sitting inside a bigger rectangular body, μ_2 is the distance between the free surface and the upper surface of the floating rectangular body, and μ_3 is the height of the rectangular body. The fact that we have introduced two parameters for the rectangular body is motivated by the fact that we aim at studying interesting limit cases (i.e., the rectangular body is degen-

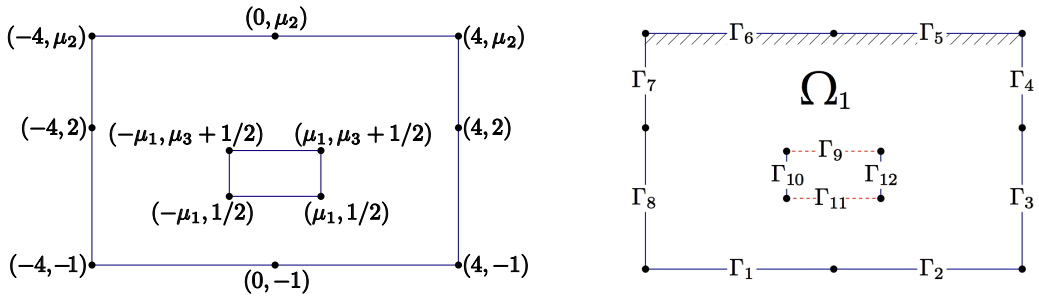

Figure 15: parametrized geometry (left) and domain boundaries (right).

erating into a lateral disk or into a transverse disk). The parameter domain is given by $\mathcal{D} = [0.5,3.5] \times [4,8] \times [0.1,3.2]$. We show in Figure 15 the boundaries of the domain. On boundaries Γ_5 and Γ_6 we impose homogeneous Dirichlet conditions $\phi(\boldsymbol{\mu}) = 0$ representing a free surface, while on boundaries Γ_1, Γ_2, Γ_3, Γ_4, Γ_7, Γ_8, Γ_{10}, and Γ_{12} we impose homogeneous Neumann conditions, $n_i \kappa_{ij} \frac{\partial}{\partial x_j} \phi(\boldsymbol{\mu}) = 0$. In addition we impose non-homogeneous Neumann conditions on the top and on the bottom of the rectangular body, respectively,

$$\frac{\partial \phi}{\partial \mathbf{n}}(\boldsymbol{\mu}) = 1 \qquad \text{on } \Gamma_9 \,, \qquad\qquad \frac{\partial \phi}{\partial \mathbf{n}}(\boldsymbol{\mu}) = -1 \quad \text{on } \Gamma_{11} \,.$$

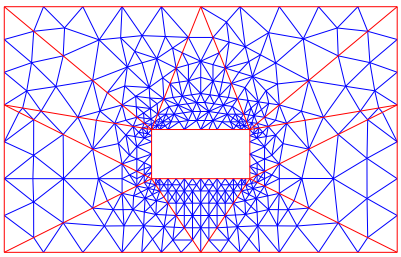

Figure 16: Finite Element Mesh

By applying Neumann non-homogeneous boundary conditions on the body surface, we obtain our output of interest, the added mass, given by

$$s(\boldsymbol{\mu}) = \int_{\Gamma_9} \phi(\boldsymbol{\mu}) - \int_{\Gamma_{11}} \phi(\boldsymbol{\mu}) \,,$$

which represents the mass of the unit density fluid moved around the body [25]. Several comparisons (and tests as limit case) have been carried out between theoretical values proposed in [25] and the ones computed with the proposed methodology for plates/disks: the computational model proves to be a very good approximation.
This problem is then modeled by the P_1 finite element (FE) discretization over the triangulation shown in Figure 16; the FE space contains $N_t = 404$ degrees of freedom. ‡.

‡ The user can obtain the RB prediction for the output and field variable (visualization) — as well as

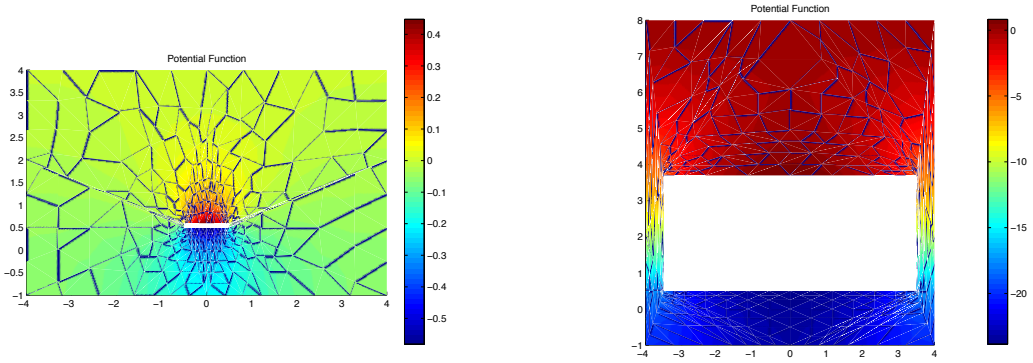

Figure 17: Representative solutions for the added mass problem $\mu = [0.5,4,0.1]$ and $\mu = [3.5,8.0,3.2]$.

12.2 Numerical results

For this problem, with $P = 3$ parameter, we visualize in Figure 18 the sample $S_{N_{\max}}$ obtained by application of the (energy version of the) greedy algorithm of Section 3.5 for Ξ_{train} a log-uniform random sample of size $n_{\text{train}} = 3000$. We may conclude with the same consideration done in section 10.2 about the clustering of sample near the boundaries of the parameter domain and the sparse sample population in the interior of the domain. We also plot in Figure 18 $\max_{\mu \in \Xi\text{train}} \left(\Delta_N^{\text{en}}(\mu) / ||\phi_N^{N_t}(\mu)||_\mu \right)$ for the Lagrange RB approximations associated with the sample on the left. We observe very rapid, exponential convergence.

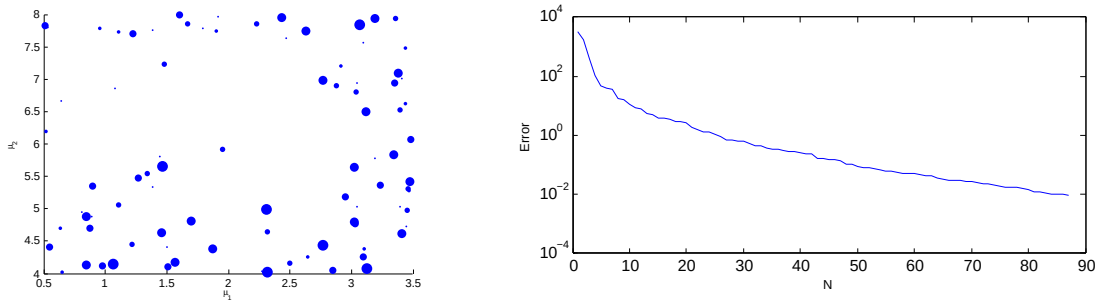

Figure 18: Added mass. Left: greedy (energy version) sample $S_{N_{\max}}$. Right: $\max_{\mu \in \Xi\text{train}} \left(\Delta_N^{\text{en}}(\mu) / ||\phi_N^{N_t}(\mu)||_\mu \right)$ as a function of N for the Lagrange RB approximations associated with the sample of Figure 18; here Ξ_{train} is a log-uniform random sample of size $n_{\text{train}} = 3000$.

---

a rigorous error bound for the real error between the RB and FE predictions — through the website `http://augustine.mit.edu/workedproblems/rbMIT/probname/F_rbMIT_probname_webserver.htm`, where `probname` is just a lable to be replaced by `venturi`, `bend` or `addedmass` in the cases taken into account in this review paper. Who wish to run on their own computers *and* who have already downloaded our rbMIT software package may also create the RB approximation by downloading the specific `Matlab` code at the link `http://augustine.mit.edu/workedproblems/rbMIT/probname/rbMIT_data/rbU_probname.m`.

13 Conclusion

We have studied some applications of reduced basis methodology to potential flows in parametrized geometries with also a special attention to domains with curved boundaries of interest for internal flows. All the crucial elements concerning problem parametrization have been introduced and generalized. Special error bounds for velocity and pressure have been proposed, also pointwise in the internal domain coming from the general error bound on the potential solution. Demonstrative results underline the versatility of the proposed methology in the solution of flows in parametrized complex geometries. The error bounds on velocity and pressure (recovered by Bernoulli theorem) provide an example of versatility of the methodology in computing also quantities related with the gradient of the solution.

14 Acknowledgements

A deep acknowledgement to Prof. A.T. Patera for very helpful discussions, suggestions, insights and remarks. I acknowledge Dr. D.B.P. Huynh and Dr. C. N. Nguyen, codeveloper of the library `rbMIT`, for their remarks and helpful discussions. I thank Prof. A. Quarteroni for his support and advise and the Progetto Roberto Rocca (Politecnico di Milano – MIT).

References

[1] B.O. Almroth, P. Stern, and F.A. Brogan. Automatic choice of global shape functions in structural analysis. *AIAA Journal*, 16:525-528, 1978.

[2] Reduced Basis at MIT. `http://augustine.mit.edu/methodology.htm`. *MIT, Cambridge*, 2007–2010. ©Massachusetts Institute of Technology.

[3] E. Balmes. Parametric falies of reduced finite element models. theory and applications. *Mechanical Systems and Signal Processing*, 44(170):283-301, 1996.

[4] A. Barrett and G. Reddien. On the reduced basis method. *Zeitschrift für Angewandte Mathematik und Mechanik*, 75(7):543-549, 1995.

[5] J.J. Bertin. *Aerodynamics for Engineers*. Prentice Hall, 2002.

[6] T. Bui-Thanh, K. Willcox, and O. Ghattas. Model reduction for large scale systems with high-dimensional parametric input space. In *Proceedings of the 48th AIAA/ASME/ASCE/AHS/ASC structures, structural dynamics and materials conference*, volume AIAA Paper 2007-2049, 2007.

[7] H.C. Elman, D.J. Silvester, and A.J. Wathen. *Finite Elements and Fast Iterative Solvers: with Applications in Incompressible Fluid Dynamics*. Oxford university Press, 2005.

[8] J.P. Fink and W.C. Rheinboldt. On the error behavior of the reduced basis technique for nonlinear finite element approximations. *Zeitschrift für Angewandte Mathematik und Mechanik*, 63:21-28, 1983.

[9] J.P. Fink and W.C. Rheinboldt. Local error estimates for parametrized non-linear equations. *SIAM Journal on Numerical Analysis*, 22:729-735, 1985.

[10] M.A. Grepl, Y. Maday, N.C. Nguyen, and A.T. Patera. Efficient reduced-basis treatment of nonaffine and nonlinear partial differential equations. *Mathematical Modelling and Numerical Analysis*, 41(3):575-605, 2007.

[11] B. Haasdonk, M. Ohlberger, and G. Rozza. A reduced basis method for evolution schemes with parameter-dependent explicit operators. *Electronic Transactions on Numerical Analysis*, 32:145–161, 2008.

[12] D.B.P. Huynh, N.C. Nguyen, G. Rozza, and A.T. Patera. *Documentation for rbMIT Software: I. Reduced Basis (RB) for Dummies*. ©Massachusetts Institute of Technology, 2007–2010. available at `http://augustine.mit.edu` together with the rbMIT Software package.

[13] D.B.P. Huynh, G. Rozza, S. Sen, and A.T. Patera. A successive constraint linear optimization method for lower bounds of parametric coercivity and inf-sup stability constants. *Comptes Rendus de l'Académie des Sciences Paris*, Sér I 345:473-478, 2007.

[14] K. Ito and S.S. Ravindran. A reduced basis method for control problems governed by PDEs. *International Series of Numerical Mathematics*, 126:153-168, 1998.

[15] K. Ito and S.S. Ravindran. A reduced-order method for simulation and control of fluid flow. *Journal of Computational Physics*, 143(2):403-425, 1998.

[16] K. Ito and S.S. Ravindran. Reduced basis method for optimal control of unsteady viscous flows. *International Journal of Computational Fluid Dynamics*, 15:97-113, 2001.

[17] K. Ito and J.D. Schroeter. Reduced order feedback synthesis for viscous incompressible flows. *Mathematical And Computer Modelling*, 33(1-3):173-192, 2001.

[18] M.Y. Lin Lee. Estimation of the error in the reduced-basis method solution of differential algebraic equations. *SIAM Journal on Numerical Analysis*, 28:512-528, 1991.

[19] A.E. Løvgren, Y. Maday, and E.M. Rønquist. A reduced basis element method for the steady Stokes problem. *Mathematical Modelling and Numerical Analysis*, 40(3):529–552, 2006.

[20] L. Machiels, Y. Maday, I.B. Oliveira, A.T. Patera, and D.V. Rovas. Output bounds for reduced-basis approximations of symmetric positive definite eigenvalue problems. *Comptes Rendus de l'Académie des Sciences Paris*, Sér I 331(2):153-158, 2000.

[21] Y. Maday, L. Machiels, A.T. Patera, and D.V. Rovas. Blackbox reduced-basis output bound methods for shape optimization. In *Proceedings of the 12th international Domain Decomposition Conference*, 2000.

[22] Y. Maday, A.T. Patera, and D.V. Rovas. A blackbox reduced-basis output bound method for noncoercive linear problems. In J.L Lions D. Cioranescu, editor, *Nonlinear partial differential equations and their applications*, Collège de France Seminar, vol. XIV, pages 535–569. Elseviever, Amsterdam, 2002.

[23] Y. Maday, A.T. Patera, and G. Turnici. Global a priori convergence theory for reduced basis approximation of single-parameter symmetric coercive elliptic partial differential equations. *Comptes Rendus de l'Académie des Sciences Paris*, 2002.

[24] Y. Maday, A.T. Patera, and G. Turnici. A priori convergence theory for reduced-basis approximations of single-parameter elliptic partial differential equations. *Journal of Scientific Computing*, 2002.

[25] J.N. Newman. *Marine Hydrodynamics*. MIT Press, 1977.

[26] N.C. Nguyen, K. Veroy, and A.T. Patera. Certified real-time solution of parametrized partial differential equations. In S. Yip, editor, *Handbook of Materials Modeling*, pages 1523–1558. Springer, 2005.

[27] A.K. Noor. Recent advances in reduction methods for nonlinear problems. *Computers & Structures*, 13:31-44, 1981.

[28] A.K. Noor. On making large nonlinear problems small. *Computer Methods in Applied Me-*

chanics and Engineering, 34:955-985, 1982.

[29] A.K. Noor, C.M. Andresen, and J.A. Tanner. Exploiting symmetries in the modeling and analysis of tires. *Computer Methods in Applied Mechanics and Engineering*, 63:37-81, 1987.

[30] A.K. Noor, C.D. Balch, and M.A. Shibut. Reduction methods for non-linear steady-state thermal analysis. *International Journal for Numerical Methods in Engineering*, 20:1323-1348, 1984.

[31] A.K. Noor and J.M. Peters. Reduced basis technique for nonlinear analysis of structures. *AIAA Journal*, 18(4):455-462, 1980.

[32] A.K. Noor and J.M. Peters. Multiple-parameter reduced basis technique for bifurcation and post-buckling analysis of composite plates. *International Journal for Numerical Methods in Engineering*, 19:1783-1803, 1983.

[33] A.K. Noor and J.M. Peters. Recent advances in reduction methods for instability analysis of structures. *Computers & Structures*, 16:67-80, 1983.

[34] A.K. Noor, J.M. Peters, and C.M. Andersen. Mixed models and reduction techniques for large-rotation nonlinear problems. *Computer Methods in Applied Mechanics and Engineering*, 44:67-89, 1984.

[35] I.B. Oliveira and A.T. Patera. Reduced-basis techniques for rapid reliable optimization of systems described by affinely parametrized coercive elliptic partial differential equations. *Optimization and Engineering*, 8:43-65, 2007.

[36] R. L. Panton. *Incompressible Flow*. John Wiley & Sons, Inc., 3rd edition edition, 2005.

[37] A.T. Patera and G. Rozza. *Reduced Basis Approximation and A Posteriori Error Estimation for Parametrized Partial Differential Equations*. to appear in MIT Pappalardo Graduate Monographs in Mechanical Engineering, 2007. ©Massachusetts Institute of Technology, Version 1.0.

[38] J.S. Peterson. The reduced basis method for incompressible viscous flow calculations. *SIAM Journal on Scientific and Statistical Computing*, 10(4):777-786, 1989.

[39] T.A. Porsching. Estimation of the error in the reduced basis method solution of nonlinear equations. *Mathematics of Computation*, 45(172):487-496, 1985.

[40] T.A. Porsching and M.Y. Lin Lee. The reduced-basis method for initial value problems. *SIAM Journal on Numerical Analysis*, 24:1277-1287, 1987.

[41] C. Prud'homme, D.V. Rovas, K. Veroy, L. Machiels, Y. maday, A.T. Patera, and G. Turinici. Reliable real-time solution of parametrized partial differential equations. *Journal of Fluids Engineering*, 124:70-80, 2002.

[42] A. Quarteroni, G. Rozza, and A. Quaini. Reduced basis methods for optimal control of advection-diffusion problems. In W. Fitzgibbon, R. Hoppe, and J. Periaux, editors, *Advances in Numerical Mathematics*, pages 193–216. Moscow, Russia and Houston, USA, 2007.

[43] A. Quarteroni and A. Valli. *Numerical Approximation of Partial Differential Equations*. Springer-Verlag Berlin, 1997.

[44] rbMIT Library. `http://augustine.mit.edu/methodology/methodology_rbmit_system.htm`. *MIT, Cambridge*, 2007–2010. ©Massachusetts Institute of Technology.

[45] W.C. Rheinboldt. On the theory and error estimation of the reduced basis method for mulit-parameter problems. *Nonlinear Analysis, Theory, Methods and Applications*, 21(11):849-858, 1993.

[46] D.V. Rovas. *Reduced-Basis Output Bound Methods for Parametrized Partial Differential Equations*. PhD thesis, Massachusetts Institute of Technology, 2003.

[47] G. Rozza. Reduced basis methods for Stokes equations in domains with non-affine parametric dependence. *Computing and Visualization in Science*, doi:10.1007/s00791-006-0044-7,

2006.

[48] G. Rozza. *Shape Design by Optimal Flow Control and Reduced Basis Techniques: Applications to Bypass Configurations in Haemodynamics*. PhD thesis, Ecole Polytechnique Féderale de Lausanne, November 2005.

[49] G. Rozza, D.B.P. Huynh, and A.T. Patera. Reduced basis approximation and a posteriori error estimation for affinely parametrized elliptic coercive partial differential equations: application to transport and continuum mechanics. *Archives of Computational Methods in Engineering*, 15(3):229–275, 2008.

[50] G. Rozza and K. Veroy. On the stability of the reduced basis method for Stokes equations in parametrized domains. *Computer methods in applied mechanics and engineering*, 196:1244-1260, 2007.

[51] W. Schröder. *Fluidmechanik - Aachener Beiträge zur Strömungsmechanik, Band 7*. Wissenschaftsverlag Mainz in Aachen, 2004.

[52] S. Sen, K. Veroy, D.B.P. Huynh, S. Deparis, N.C. Nguyen, and A.T. Patera. "Natural norm" a posteriori error estimators for reduced basis approximations. *Journal of Computational Physics*, 217:37-62, 2006.

[53] K. Veroy and A.T. Patera. Certified real-time solutions of the parametrized steady incompressible Navier-Stokes equations. *International Journal for Numerical Methods in Fluids*, 47:773-788, 2005.

[54] K. Veroy, C. Prud'homme, D.V. Rovas, and A.T. Patera. A posteriori error bounds for reduced-basis approximation of parametrized noncoercive and nonlinear elliptic partial differential equations. In *Proceedings of the 16th AIAA computational fluid dynamics conference*, volume Paper 2003-3847, 2003.

Publications récentes

INSTITUT D'ANALYSE ET CALCUL SCIENTIFIQUE
Section de Mathématiques
Ecole Polytechnique Fédérale
CH 1015 Lausanne

05.2009 G. ROZZA, C. N. NGUYEN, A.T. PATERA, S. DEPARIS :
Reduced basis methods and a posteriori error estimators for heat transfer problems

06.2009 G. ROZZA, D.B.P. HUYNH, C.N. NGUYEN, A.T. PATERA :
Real-time reliable simulation of heat transfer phenomena

07.2009 Z. C. XUAN, T. LASSILA, G. ROZZA, A. QUARTERONI :
On computing upper and lower bounds on the outputs of linear elasticity problems approximated by the smoothed finite element method

Publications récentes

INSTITUT DE MATHEMATIQUES DES SCIENCES COMPUTATIONELLES ET INGENIERIE
Section de Mathématiques
Ecole Polytechnique Fédérale
CH 1015 Lausanne

01.2010 G. ROZZA, T. LASSILA :
Parametric free-form shape design with PDE models and reduced basis method

02.2010 G. ROZZA, T. LASSILA, A. MANZONI :
Reduced basis approximation for shape optimization in thermal flows with a prametrized polynomial geometric map

03.2010 A. CABOUSSAT, J. RAPPAZ:
Numerical simulation of bubbles under an inclined plane: application to aluminum electrolysis

04.2010 J. DESCLOUX, M. FLÜCK, J. RAPPAZ :
Modelling and mathematical results arising from ferromagnetic problems

05.2010 G. ROZZA, A. MANZONI :
Model order reduction by geometrical parametrization for shape optimization in computational fluid dynamics

06.2010 S. DEPARIS, A. E. LØVGREN :
Stabilized reduced basis approximation of incompressible three-dimensional Navier-Stokes equations in parametrized deformed domains

07.2010 P. CROSETTO, PH. REYMOND, S. DEPARIS, D. KONTAXAKIS, N. STERGIOPULOS, A. QUARTERONI :
Fluid structure interaction simulations of physiological blood flow in the aorta

08.2010 P. CROSETTO, S. DEPARIS, G. FOURESTEY, A. QUARTERONI :
Parallel algorithms for fluid-structure interaction problems in haemodynamics

09.2010 A. CABOUSSAT, P. CLAUSEN, J. RAPPAZ :
Numerical simulation of two-phases flow with interface tracking by adaptive Eulerian grid subdivision

10.2010 J. BONNEMAIN :
From medical images to numerical simulations

11.2010 G. ROZZA :
Reduced basis approximation and error bounds for potential flows in parametrized geometries